Journal of Structural Geology 97 (2017) 71–92

Contents lists available at ScienceDirect

Journal of Structural Geology

journal homepage: www.elsevier.com/locate/jsg

High-velocity frictional properties of Alpine Fault rocks: Mechanical data, microstructural analysis, and implications for rupture propagation

Carolyn Boulton [a, b, *], Lu Yao [c], Daniel R. Faulkner [b], John Townend [d], Virginia G. Toy [e], Rupert Sutherland [f, d], Shengli Ma [c], Toshihiko Shimamoto [c]

[a] Department of Geological Sciences, University of Canterbury, Christchurch, New Zealand
[b] School of Environmental Sciences, University of Liverpool, Liverpool, United Kingdom
[c] State Key Laboratory of Earthquake Dynamics, Institute of Geology, China Earthquake Administration, Beijing, China
[d] School of Geography, Environmental, and Earth Sciences, Victoria University of Wellington, Wellington, New Zealand
[e] Department of Geology, University of Otago, Dunedin, New Zealand
[f] GNS Science, Lower Hutt, New Zealand

ARTICLE INFO

Article history:
Received 7 August 2016
Received in revised form
30 January 2017
Accepted 9 February 2017
Available online 11 February 2017

Keywords:
Alpine fault
High-velocity friction
Fracture energy
Rupture propagation
Microstructures
Shear bands

ABSTRACT

The Alpine Fault in New Zealand is a major plate-bounding structure that typically slips in ~M8 earthquakes every c. 330 years. To investigate the near-surface, high-velocity frictional behavior of surface- and borehole-derived Alpine Fault gouges and cataclasites, twenty-one rotary shear experiments were conducted at 1 MPa normal stress and 1 m/s equivalent slip velocity under both room-dry and water-saturated (wet) conditions. In the room-dry experiments, the peak friction coefficient ($\mu_p = \tau_p/\sigma_n$) of Alpine Fault cataclasites and fault gouges was consistently high (mean $\mu_p = 0.67 \pm 0.07$). In the wet experiments, the fault gouge peak friction coefficients were lower (mean $\mu_p = 0.20 \pm 0.12$) than the cataclasite peak friction coefficients (mean $\mu_p = 0.64 \pm 0.04$). All fault rocks exhibited very low steady-state friction coefficients (μ_{ss}) (room-dry experiments mean $\mu_{ss} = 0.16 \pm 0.05$; wet experiments mean $\mu_{ss} = 0.09 \pm 0.04$). Of all the experiments performed, six experiments conducted on wet smectite-bearing principal slip zone (PSZ) fault gouges yielded the lowest peak friction coefficients ($\mu_p = 0.10–0.20$), the lowest steady-state friction coefficients ($\mu_{ss} = 0.03–0.09$), and, commonly, the lowest specific fracture energy values ($E_G = 0.01–0.69$ MJ/m^2). Microstructures produced during room-dry and wet experiments on a smectite-bearing PSZ fault gouge were compared with microstructures in the same material recovered from the Deep Fault Drilling Project (DFDP-1) drill cores. The near-absence of localized shear bands with a strong crystallographic preferred orientation in the natural samples most resembles microstructures formed during wet experiments. Mechanical data and microstructural observations suggest that Alpine Fault ruptures propagate preferentially through water-saturated smectite-bearing fault gouges that exhibit low peak and steady-state friction coefficients.

1. Introduction

The Alpine Fault, South Island, New Zealand is a long-lived crustal-scale continental transform fault that has accommodated at least 460 km of cumulative displacement in the past c. 45 Myr (Wellman, 1953; Sutherland et al., 2000). Paleoseismological records indicate that the Alpine Fault produces quasi-periodic large-magnitude (M~8) earthquakes that propagate along-strike for 300–600 km (Wells and Goff, 2007; Sutherland et al., 2007; Berryman et al., 2012). Single-event strike-slip and dip-slip surface displacements on the Alpine Fault are 7.5–9 m and c. 1 m, respectively (Barth et al., 2013). Boulton et al. (2012) and Barth et al. (2013) measured the frictional strength and stability of smectitic principal slip zone (PSZ) gouges from well-studied localities spanning c. 220 km along strike of the central and southern Alpine Fault. They concluded that the velocity-strengthening frictional properties of surface-outcrop PSZ gouges tested while fluid-saturated at

* Corresponding author. School of Environmental Sciences, University of Liverpool, Liverpool, United Kingdom.
E-mail address: carolyn.boulton@liverpool.ac.uk (C. Boulton).

http://dx.doi.org/10.1016/j.jsg.2017.02.003

room temperature and low sliding velocities (v < 100–300 μm/s) were incompatible with paleoseismological and geomorphological evidence for surface-rupturing earthquakes. Subsequent hydrothermal experiments at close to in situ conditions comparable to 2–8 km depth showed that central Alpine Fault gouges do have the velocity-weakening properties required for earthquake nucleation (Boulton et al., 2014; Niemeijer et al., 2016).

Dynamically, a large (≥3-fold) reduction in the coefficient of friction of both intact and granular rocks during high-velocity sliding (v > 0.1 m/s) has been observed repeatedly since the first rotary shear experiments by Tsutsumi and Shimamoto (1997) (for reviews, see Wibberley et al., 2008; Di Toro et al., 2011; Niemeijer et al., 2012). A wide range of dynamic weakening mechanisms has been proposed to explain this effect, including: melt lubrication (e.g., Hirose and Shimamoto, 2005; Nielsen et al., 2008), silica gel lubrication (Goldsby and Tullis, 2002; Di Toro et al., 2004), flash heating (Rice, 2006; Beeler et al., 2008; Goldsby and Tullis, 2011), powder lubrication (e.g., Han et al., 2010; Reches and Lockner, 2010; Chang et al., 2012), fluid film lubrication (Brodsky and Kanamori, 2001; Ferri et al., 2011), and thermal pressurization (e.g., Sibson, 1973; Lachenbruch, 1980; Wibberley and Shimamoto, 2005; Rice, 2006; Sulem et al., 2007; Tanikawa and Shimamoto, 2009; Faulkner et al., 2011) or thermochemical pressurization (Brantut et al., 2008, 2011; Chen et al., 2013; Platt et al., 2015). To what extent hanging wall, principal slip zone (PSZ), and footwall Alpine Fault rocks undergo high-velocity weakening remains untested.

The present study documents the results of room-dry and water-saturated high-velocity, low-normal stress (v = 1 m/s, σ_n = 1 MPa) friction experiments conducted on Alpine Fault gouge and cataclasite samples collected from the surface at Gaunt Creek and Hokuri Creek, and from shallow depths during the Deep Fault Drilling Project (DFDP-1) at Gaunt Creek (Fig. 1). A focus of these experiments is to quantify the peak coefficient of friction (μ_p), as this value represents the yield strength and thus a barrier to rupture propagation. An additional aim is to quantify the steady-state coefficient of friction (μ_{ss}) at high velocity as well as the slip-weakening distance (d_w) over which μ_{ss} is reached. Finally, microstructures produced during six experiments with varying velocity histories and pore-fluid conditions are compared with microstructures formed in naturally occurring smectitic PSZ fault gouges. By doing so, we test: (1) the effect pore fluids have on microstructural evolution during high-velocity sliding; (2) the effect decelerating slip and simulated afterslip have on recovered experimental microstructures, and (3) the degree to which natural microstructures resemble those produced during experimental deformation. Our results allow us to conclude that small variations in sliding velocity following a high-velocity slip event have little effect on microstructures recovered and that natural microstructures resemble those formed during wet high-velocity friction experiments.

2. Fault rock descriptions

2.1. Analytical methods

Samples were collected from unoriented drill core retrieved during the first phase of the Deep Fault Drilling Project (DFDP-1) at Gaunt Creek (hereafter GC) (Fig. 1). An additional sample of PSZ gouge was collected from a nearby outcrop (the GC scarp outcrop of Boulton et al., 2012). All sample depths reported from DFDP-1B are adjusted by +0.20 m from borehole lithological logs following Townend et al. (2013). Saponite-rich gouge collected from a 12 m-wide PSZ at Hokuri Creek (HkC PSZ) on the southern Alpine Fault was also tested. The gouge mineralogy, microstructure, and low-velocity frictional and hydrological properties of the HkC PSZ gouge were described in detail by Barth et al. (2013). With the exception of the DFDP-1B 144.04 m gouge, all samples were gently disaggregated using mortar and pestle, and the powdered material was passed through a 100# sieve to obtain a <150 μm separate. Quantitative X-ray diffraction (XRD) analyses were undertaken to determine the mineralogy of each sieved DFDP separate and the bulk rock mineralogy of the DFDP-1B 144.04 m gouge, which was tested without sieving due to the limited quantity of material available.

2.2. Fault rock occurrence, nomenclature, and mineralogy

Brief descriptions of the eight fault rock samples used in high-velocity friction experiments are presented here following the lithologic units described by Toy et al. (2015a). Core-scale images of the DFDP-1 samples are illustrated in Fig. 1. High-velocity friction experiments were performed on two Unit 4 foliated cataclasites (DFDP-1A 86.41 m and DFDP-1A 90.32 m), one Unit 6 cataclasite (DFDP-1B 128.80 m), and four Unit 5 gouges (DFDP-1A 90.62 m, DFDP-1B 128.44 m, DFDP-1B 144.04 m, and GC Scarp PSZ) (cf. Fig. 5b,d and f in Toy et al., 2015). Hokuri Creek fault gouge (HkC PSZ) was also deformed (cf. Fig. 6c,f,i and l in Barth et al., 2013). Henceforth, DFDP-1 samples are referred to by hole (1A or 1B), depth below top of the hole (m), and fault rock lithology (foliated cataclasite, gouge, or cataclasite).

In the DFDP-1 boreholes, hanging wall lithologic units 2, 3, and 4 occur within the fault core; these units have formed due to alteration (Unit 2, 3, and 4) and brittle fragmentation, translation, and rotation (Units 3 and 4) of Unit 1 quartzofeldspathic and metabasic ultramylonites (Sutherland et al., 2012; Toy et al., 2015a; Boulton et al., 2017). The Unit 4 foliated cataclasite samples tested contain irregularly spaced planar to locally anastomosing seams of aligned phyllosilicates (Fig. 1d and e). The Unit 6 cataclasite comprises comminuted quartz-plagioclase-potassium feldspar granitoid aggregates and rare gneiss clasts (Fig. 1f). The Unit 5 gouges are incohesive fault rocks with >90% matrix grains <0.1 mm in size. Unit 5 gouges can be differentiated by phyllosilicate mineralogy (described below) and the nature and abundance of protolith clasts. 1A 90.62 m gouge contains ultramylonite and cataclasite clasts, calcite vein fragments, and rare clasts, lenses, or veins of underlying smectitic gouge (Fig. 1e) (see also Boulton et al., 2014).

Compared to the 1A 90.62 m gouge, 1B 128.44 m (PSZ-1) gouge has a higher proportion of gouge clasts relative to cataclasite and ultramylonites clasts and fewer calcite vein fragments (Fig. 1f). In drill core, the 1B 128.44 m gouge is c. 20 cm-thick, and its contact with the hanging wall was not recovered. In two thin sections, one unoriented and one cut subparallel to a slickenside lineation, the PSZ-1 gouge exhibits reverse grading with distance from its contact with the underlying footwall cataclasite. Near the footwall contact, microstructures include a random-fabric matrix (Fig. 2a) with a single fault-parallel (Y-shear) shear band <50 μm-thick (Fig. 2c and d). The 1B 144.04 m (PSZ-2) gouge contains clasts of gneiss, ultramylonite, gouge and quartz-feldspar-plagioclase aggregate (Figs. 1g and 2b). In drill core, the 1B 144.04 m gouge is c. 10-cm thick and both its hanging wall and footwall contacts were recovered. In an unoriented thin section, the PSZ-2 gouge comprises a random fabric with anastomosing but discontinuous shear bands developed locally adjacent to competent hanging wall and footwall cataclasites (Fig. 2e and f). There is no evidence of continuous shear band(s) with a crystallographic preferred orientation. GC Scarp PSZ gouge clasts include reworked fault gouge, cataclasite, calcite vein fragments, metamorphic quartz, and vein quartz; the outcrop was described by Boulton et al. (2012).

Table 1 lists the mineralogy of each fault rock <150 μm separate; note the 1B 144.04 m gouge was not sieved. All fault rocks analyzed

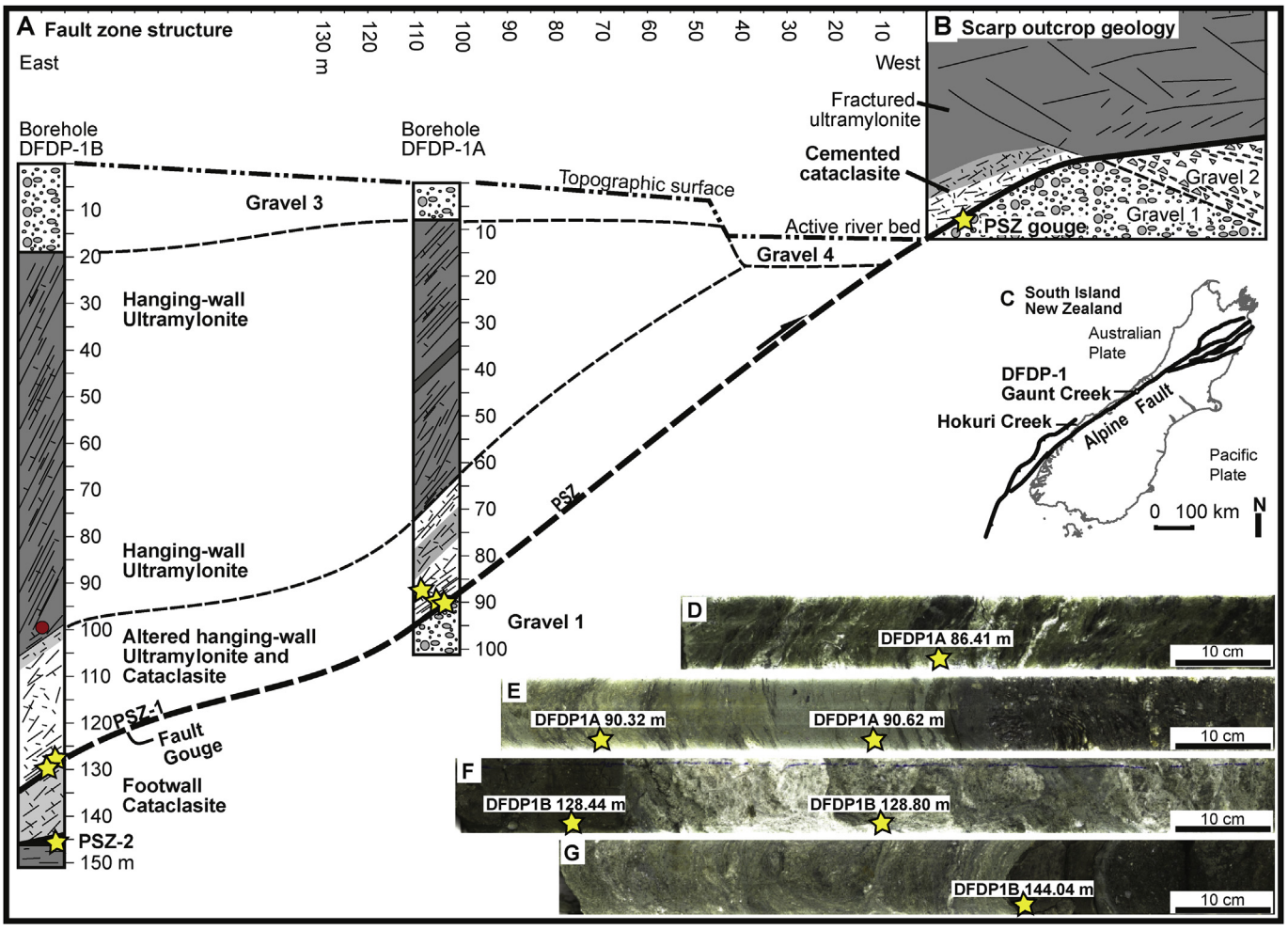

Fig. 1. (a) Schematic cross-section of Alpine Fault geology in boreholes DFDP-1A and DFDP-1B, drilled at Gaunt Creek (GC). Yellow stars indicate the location of fault rock samples investigated; a red circle indicates the location of pseudotachylyte imaged in Fig. 12. The upper dashed line demarcates the boundary of the alteration zone-fault core, as defined by the first occurrence of altered ultramylonite. PSZ denotes principal slip zone. (b) Schematic cross-section of Alpine Fault geology in a scarp outcrop on the southern side of Gaunt Creek. Experimental sample GC Scarp PSZ gouge was collected from this locality (star). (c) Location map of Alpine Fault sample localities discussed in the text (Fig. 1a,b, and c modified after Sutherland et al., 2012). (d) 180° core scan of DFDP-1A Run 63_2, from which 1A 86.41 m foliated cataclasite was collected. (e) 180° core scan of DFDP-1A Run 66_2, from which 1A 90.32 m foliated cataclasite and 1A 90.62 m fault gouge were collected. (f) 180° core scan of DFDP-1B Run 59_1, from which the 1B 128.44 m gouge and 1B 128.80 m cataclasite were collected. (g) 180° core scan of DFDP-1B Run 69_2, from which 1B 144.04 m gouge was collected. (For interpretation of the references to colour in this figure legend, the reader is referred to the web version of this article.)

are polymineralic, and it is known that the presence of phyllosilicate minerals influences frictional strength (e.g., Byerlee, 1978; Shimamoto and Logan, 1981; Ikari et al., 2009; Tembe et al., 2010). The fault rocks studied are classified as phyllosilicate-poor (<20%) or phyllosilicate-rich (≥20% phyllosilicates) following Shimamoto and Logan (1981), who observed that the addition of ≥15–20% smectite to smectite-anhydrite mixtures resulted in frictional weakness. The presence of the weak phyllosilicate mineral smectite also influences high-velocity frictional behaviors (e.g., Bullock et al., 2015), and this is noted in the text and figures that follow. 1A 86.41 m foliated cataclasite and 1B128.80 m cataclasite are phyllosilicate-poor. 1A 90.32 m foliated cataclasite, 1A 90.62 m gouge, 1B 128.44 m gouge, 1B 144.04 m gouge, GC Scarp PSZ gouge and HkC PSZ gouge are phyllosilicate-rich (Table 1). The 1B 128.44 m, 1B144.04 m, GC Scarp PSZ, and HkC PSZ gouges are also smectitic. Quantitative XRD analysis of the HkC PSZ gouge <150 μm separate was not done because whole rock and 2 μm separate XRD analyses of the gouge revealed that mineralogy did not vary considerably (Table 1). The smectite mineral saponite comprise 74% of the whole rock and 78% of the 2 μm separate; thus, the <150 μm separate likely contains 74–78% saponite.

3. High-velocity friction experiments

3.1. Experimental procedure

High-velocity friction experiments (HVFE) were conducted using the low to high velocity (LHV) friction apparatus at the State Key Laboratory of Earthquake Dynamics, Institute of Geology, China Earthquake Administration, Beijing, China (cf. Fig. 2 of Ma et al., 2014). Experimental procedures followed the method outlined by Mizoguchi et al. (2007). In each experiment, an air actuator applied an axial force of 1.25 kN to a solid cylindrical sample of 40 mm diameter, yielding an applied normal stress (σ_n) of 0.995 MPa which remained constant to within ±0.004 MPa (inset Fig. 3). In Table 2, normal stress in each experiment is reported as 1.0 MPa. The effect of pre-compacting HkC PSZ gouge at σ_n = 2.0 MPa was tested in room dry experiment LHV262. Prior to imposing shear, samples were left under load until the displacement transducer recorded a steady-state thickness, typically within less than 1 h.

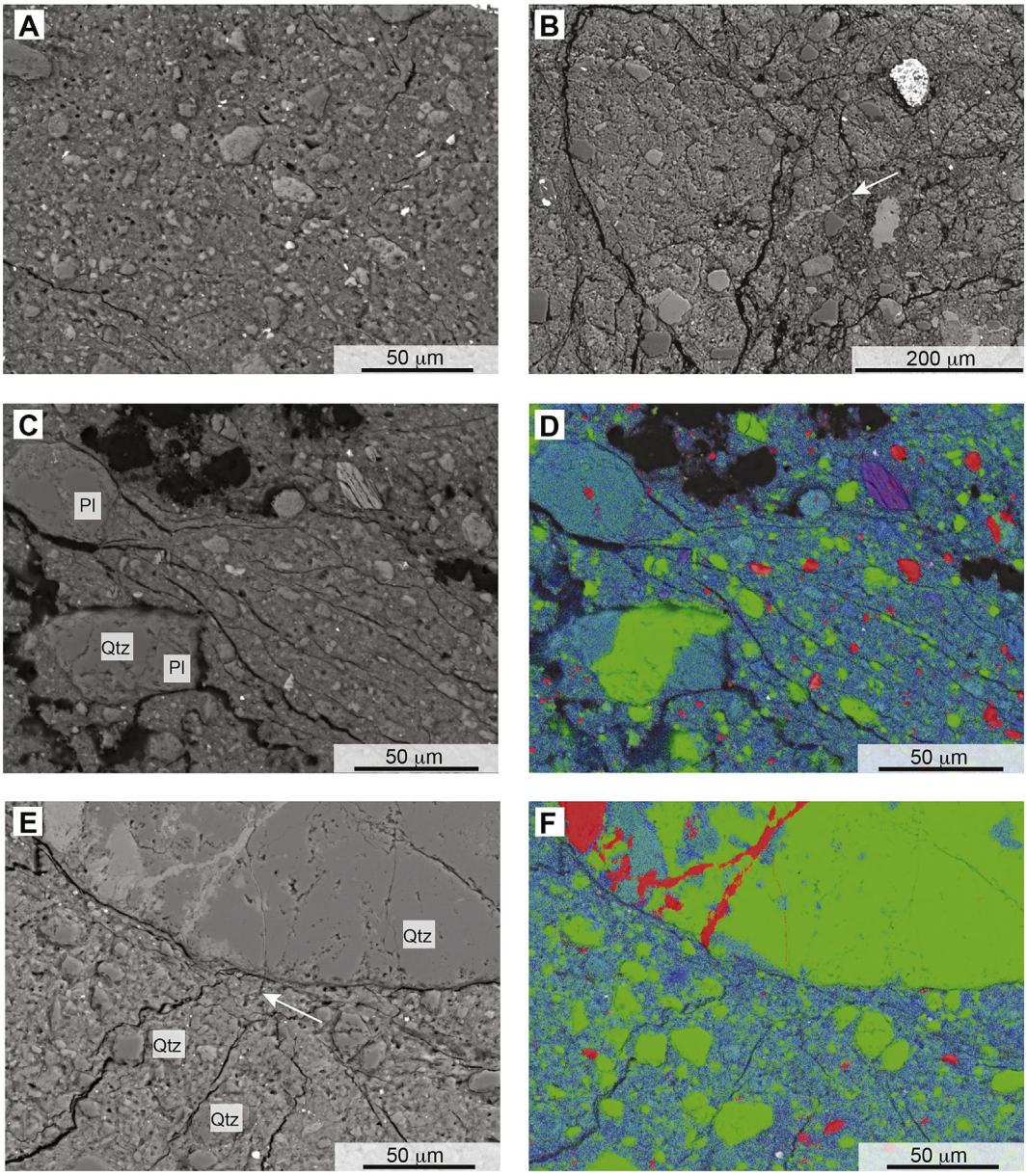

Fig. 2. Representative microstructures within drill-core thin sections at DFDP-1B 128.44–128.49 m (PSZ-1) and DFDP-1B 144.04–144.14 m (PSZ-2). (a) Backscattered electron (BSE) image of random gouge fabric in DFDP-1B PSZ-1. Grains display no shape-preferred orientation. (b) BSE image of a fault gouge clast within a low-strain region in DFDP-1B PSZ-2. Note the compacted calcite vein oriented sub-perpendicular to the fault plane (arrow). The bright grain in the top-right corner is a clast coated in skeletal Ti-oxide. (c) BSE image of DFDP-1B PSZ-1 phyllosilicates aligned locally in the wake of rigid grains of plagioclase (Pl) and quartz (Qtz), forming a localized shear band mapped in (d), an EDS element map, and imaged again in Fig. 12e–f. In all EDS element maps, red is calcium (usually in the mineral calcite), green is silica (which occurs most abundantly in quartz), and blue is aluminum (which occurs most abundantly in phyllosilicates or in variable amounts within plagioclase and K-feldspar). (e–f) BSE image and EDS element map of phyllosilicates in DFDP-1B PSZ-2 forming a thin, discontinuous shear band adjacent to a rigid quartz-calcite clast (arrow). Other grains within the gouge matrix display no shape-preferred orientation. (For interpretation of the references to colour in this figure legend, the reader is referred to the web version of this article.)

To induce shear, a 22 kW servo-motor rotated one side of the sample assembly while the other side was kept stationary. Velocity varies with radial position on solid cylindrical samples, and the equivalent slip velocity (v_{eq} in ms^{-1}) is calculated as follows:

$$v_{eq} = \frac{4\pi R r_0}{3} \quad (1)$$

where r_0 is the outer radius and R is the revolution speed in revolutions per second. Equivalent slip velocity is here defined such that the rate of frictional work is $\tau v_{eq} S$ if the shear stress is assumed to be constant over the sliding surface of area S (Shimamoto and Tsutsumi, 1994; Mizoguchi et al., 2007). For a full analysis of the assumption that normal stress and shear stress acting on the sample is uniform, i.e., that the coefficient of friction is independent of position in the sample, see Kitajima et al. (2010). Most HVFEs listed in Table 2 were conducted at a v_{eq} of 1.0 m/s. After the initial acceleration to 1.0 m/s, which occurred within 0.16 ± 0.03 s, v_{eq} varied by less than 0.0004 m/s during the experiment. Velocity history was varied in four experiments on 1B 128.44 m gouge. In 2 experiments, termed high-velocity friction experiments with decelerating slip (HVFE with decelerating slip), deceleration was programmed to occur over the last 1 m of slip. In another two experiments, termed high-velocity friction experiments with afterslip

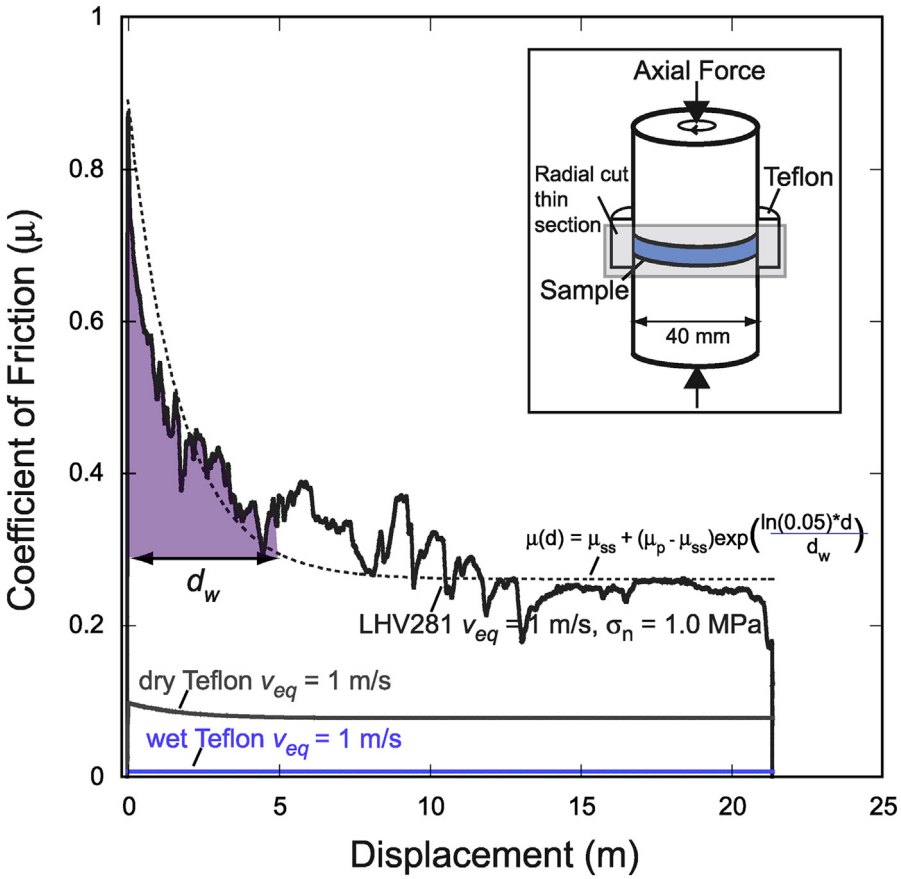

Fig. 3. Plot of the uncorrected coefficient of friction (μ) vs. displacement (d) for the room-dry high velocity friction test conducted on 1A 86.41 m foliated cataclasite (LHV281). The coefficient of friction was calculated from the ratio of recorded shear stress (τ) to recorded normal stress (σ_n). It should be assumed that the effective normal stress ($\sigma_n'=\sigma_n-P_p$) in the sample is lower because of some amount of pore pressure, which could not be measured experimentally. The slip-weakening distance (d_w) was determined by fitting Equation (2) to the raw data. Specific fracture energy (E_G) (shaded region) was calculated by the integral of the raw friction data multiplied by the applied normal stress. Also plotted is the frictional strength of dry Teflon® (grey line) and wet Teflon® (blue line). Inset figure depicts the sample assembly and location of the radially cut thin section. (For interpretation of the references to colour in this figure legend, the reader is referred to the web version of this article.)

(HVFE with afterslip), samples were sheared for 20 m at $v_{eq} = 1$ m/s, decelerated over 0.45 m of slip, and sheared for a further 1 m at $v_{eq} = 0.001$ m/s. Torque, axial force, axial displacement, and rotary motion data were recorded at a sampling rate of either 200 Hz or 500 Hz.

Each sample assembly comprised two cylinders of Shanxi gabbro, a Teflon® sleeve, and 2.5 g of room-dry (dry) < 150 μm fault rock separate (the 1B 144.04 m gouge was not sieved). Fault rock powders were placed between two 39.980–39.990 mm-diameter Shanxi gabbro cylinders (permeability < 10^{-22} m^2) with sliding surfaces ground on a 150# (100 μm) diamond-grinding wheel to make them planar. Sliding surfaces were also roughened with 80# SiC (180 μm) to inhibit slippage along the interface. Each fault rock powder was contained by a Teflon® sleeve with an inner diameter 135–180 μm smaller than the gabbro cylinders (inset Fig. 3). Relative humidity in the laboratory ranged between 40% and 60%. Initial sample thickness ranged between 1.0 mm and 1.3 mm. For the water-saturated (wet) experiments, 0.625 mL (25 wt%) of deionized water was added to the fault rock powder. To allow the water to permeate the sample, it was sheared one full rotation in 3 min under 0.477 MPa normal stress. The normal stress was then increased to 1.0 MPa prior to the experiment. It was not feasible to measure directly the pore-fluid pressure during the high-velocity water-saturated experiments. Chen et al. (2013) used numerical modeling to estimate the initial pore-fluid pressure and obtained a value of approximately 0.10–0.20 MPa.

Using Teflon® sleeves to confine the gouge is necessary but undesirable because they contribute to the total torque measurement, fluctuate in torque because of sample assembly misalignment, decompose to release a highly reactive fluorine gas, and wear to produce small particles that mix with the sample (e.g., Kitajima et al., 2010; Sawai et al., 2012). To minimize torque fluctuations, upper and lower portions of the sample assembly were aligned to within 1 μm prior to each experiment. Pungent gas and black grooves in the Teflon® sleeves indicate that decomposition occurred at temperatures ≥260 °C during the dry experiments (http://www2.dupont.com/Teflon_Industrial/en_US/tech_info/prodinfo_ptfe.html). In wet experiments, the Teflon® sleeves showed no signs of wear or decomposition. Kitajima et al. (2010) found that Teflon® particles are unlikely to affect the coefficient of friction because they are typically present in insignificant amounts.

To account for the contribution of the room-dry and water-saturated Teflon® to the total torque, two experiments were conducted in which the sample assembly, without gouge, was sheared at $v_{eq} = 1.0$ m/s and $v_{eq} = 0.001$ m/s without the gabbro cylinders touching. At $v_{eq} = 1.0$ m/s, dry Teflon® had an apparent peak shear stress of 0.097 MPa, which decayed exponentially to a steady-state shear stress of 0.077 MPa; at $v_{eq} = 0.001$ m/s, dry Teflon® had a constant apparent shear stress of 0.031 MPa. Wet Teflon® displayed a constant apparent shear stress of 0.007 MPa at both velocities tested (Fig. 3). The values of the peak coefficient of friction (μ_p) and

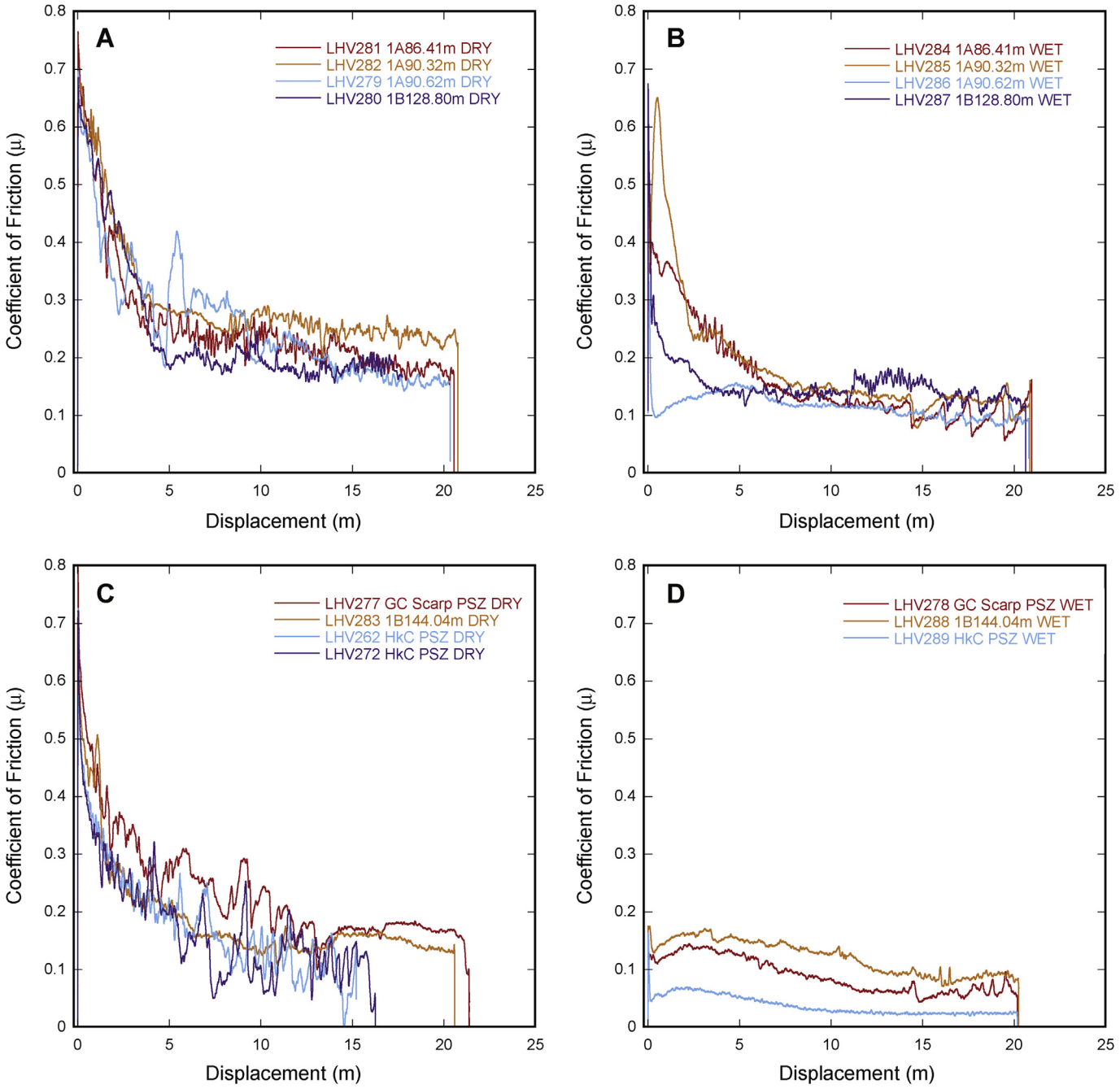

Fig. 4. Coefficient of friction data recorded during dry and wet LHV200-series high-velocity experiments. (a,b) coefficient of friction vs. displacement results for dry and wet experiments conducted on 1A86.41 m foliated cataclasite, 1A 90.32 m foliated cataclasite, 1A 90.62 m gouge, and 1B 128.80 m cataclasite. (c,d) coefficient of friction vs. displacement results for dry and wet experiments conducted on smectitic PSZ gouges GC Scarp PSZ, 1B 144.04 m, and HkC PSZ. Experiment LHV262 was pre-compacted under 2 MPa normal stress.

steady state coefficient of friction (μ_{ss}) reported in Table 2 have been corrected for Teflon® friction. Subtracting the contribution of Teflon® to total torque recorded nowhere results in a negative coefficient of friction. In Figs. 4 and 5, dry slip-weakening curves were corrected for Teflon® friction following the method of Togo et al. (2011). A constant Teflon® friction correction was applied to all wet slip-weakening curves and to the dry HVFE with afterslip data collected at $v_{eq} = 0.001$ m/s. For a more detailed discussion about Teflon® friction, see the appendix of Sawai et al. (2012).

3.2. Data analysis

Published results confirm that the relationship between shear stress and normal stress follows Amonton's Law for dry high-velocity friction experiments in the absence of melt (Ujiie and Tsutsumi, 2010; Di Toro et al., 2011; Sawai et al., 2012; Yao et al., 2013a). Therefore, the coefficient of friction (μ) is taken to equal the ratio of shear stress (τ) to normal stress (σ_n). In the experiments performed on the LHV apparatus, it was not possible to measure pore-fluid pressure, gas emissions, or temperature within the slip zone. All coefficient of friction values should be considered

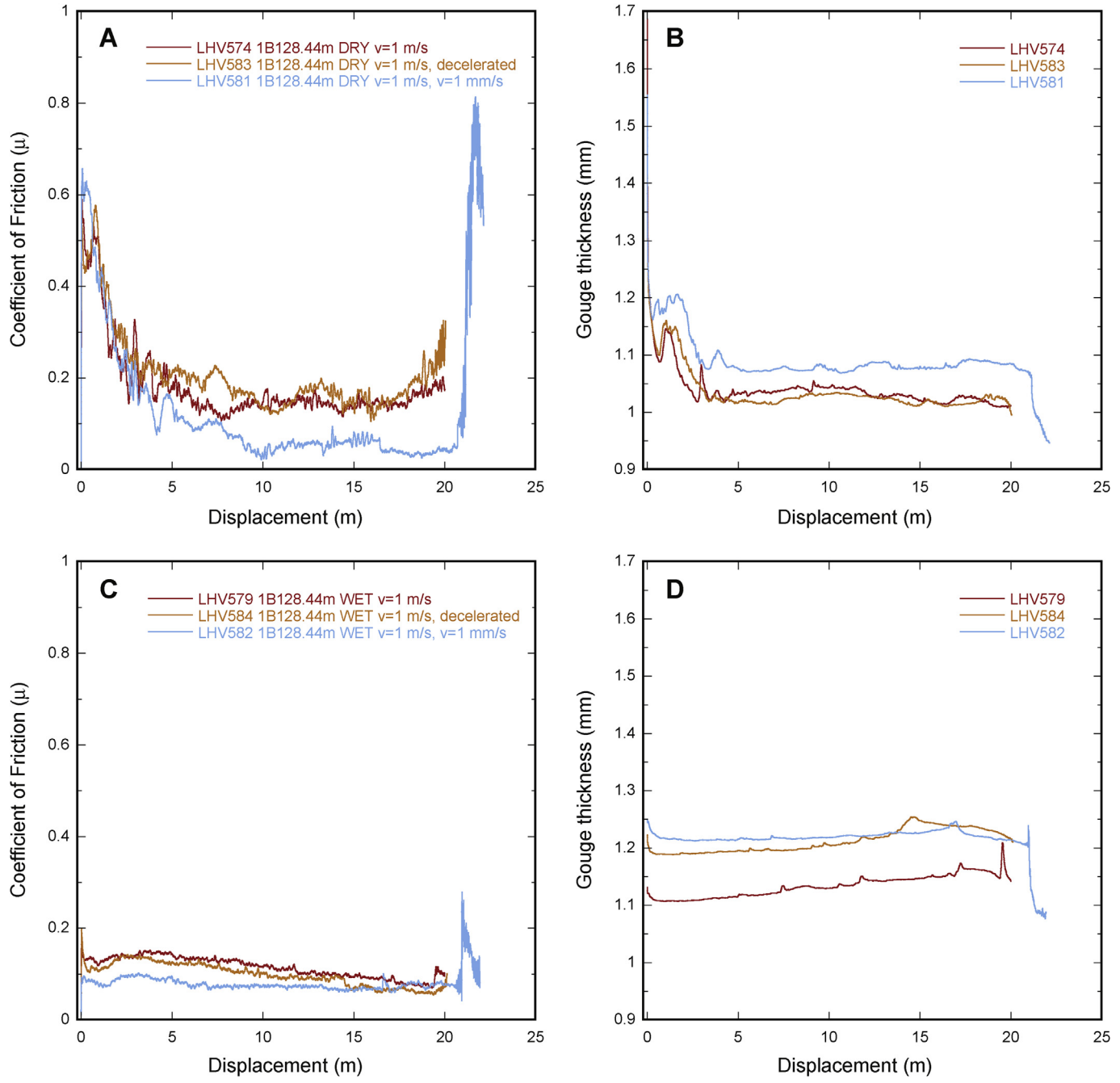

Fig. 5. Coefficient of friction and gouge thickness data recorded during the dry and wet high-velocity friction experiments on 1B 128.44 m gouge (PSZ-1). (a,b) coefficient of friction vs. displacement and gouge layer thickness vs. displacement results for dry experiments. Decreases in gouge thickness indicate compaction; increases in gouge thickness indicate dilation. Changes in gouge thickness were calculated from axial displacement data, which may include a small component (up to 0.02 mm) of dilation due to thermal expansion of gabbro wall rocks (Kitajima et al., 2010). (c,d) coefficient of friction vs. displacement and gouge layer thickness vs. displacement results for wet experiments.

apparent values because the possible effects of pore-fluid pressurization due to compaction, mineral dehydration, decarbonation, and shear heating are not quantifiable. Nevertheless, experimental results are presented in terms of the coefficient of friction to facilitate comparison with other experiments conducted at different normal stresses.

To describe the relationship between displacement and the coefficient of friction, slip weakening curves for raw dry and wet data were fit with the following negative exponential equation:

$$\mu(\mathrm{d}) = \mu_{ss} + \left(\mu_p - \mu_{ss}\right) \exp\left(\frac{\ln(0.05)\cdot d}{d_w}\right) \quad (2)$$

where μ is the coefficient of friction, μ_{ss} is the steady state coefficient of friction, μ_p is the peak coefficient of friction, d is displacement after the peak friction coefficient, and d_w is the displacement at which $(\mu_p - \mu_{ss})$ reduces to 5% of $(\mu_p - \mu_{ss})$ (Mizoguchi et al., 2007) (inset, Fig. 3). To avoid confusion with d_c in the rate and state friction equations (Marone, 1998), d_w rather than D_c is used to

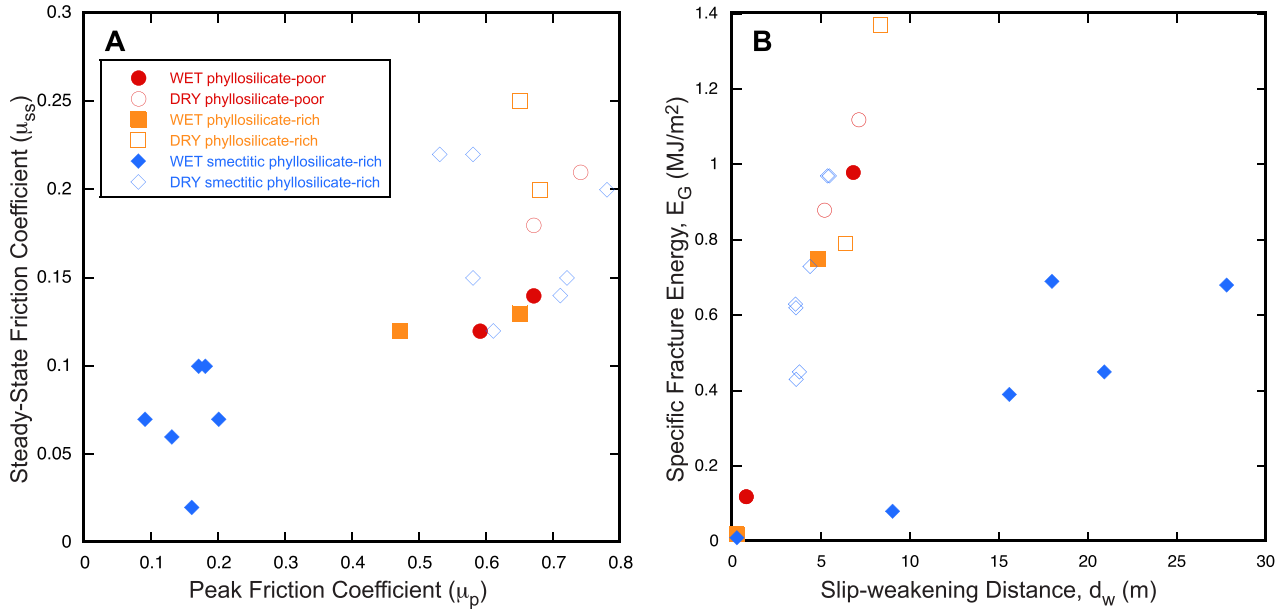

Fig. 6. (a) A plot of state-state friction coefficient (μ_{ss}) vs. peak friction coefficient (μ_p) for all experiments. All data have been corrected for Teflon® friction. (b) A plot of specific fracture energy (E_G) vs. slip-weakening distance (d_w) for all experiments. Legend for (b) is the same as for (a). Samples 1A 86.41 m and 1B 128.80 m are phyllosilicate-poor. Samples 1A 90.32 m and 1A 90.62 m are phyllosilicate-rich, but not smectitic. Samples GC Scarp PSZ, 1B 128.44 m, 144.04 m, and HkC PSZ are phyllosilicate-rich and smectitic.

Table 1
Quantitative X-ray diffraction data for high-velocity friction experiment materials. Lithologies are the lithological units defined in Toy et al. (2015a).

Hole Depth/Sample	Lithology	Quartz	K Feldspar	Plagioclase	Calcite	Kaolinite	Smectite	White mica	Chlorite	Serpentine[c]	Talc	% Phyllosilicates
1A 86.41 m	4	31	22	28	5	1		12	5			18
1A 90.32 m	4	44	6	9	4			30	4			34
1A 90.62 m	5	28	40	6	12			8	12			20
1B 128.44 m	5	22	15	21	10		26[a]	5	1			32
1B 128.80 m	6	31	20	30	1			15	1			16
1B 144.04 m*	5	36	4	23	5		15[a]	15	2			32
GC Scarp PSZ	5	29	21	20	5		14[a]	10	5			29
HkC PSZ WR	5	2	5				74[b]		3	12	2	91
HkC PSZ < 2 μm	5						78[b]			21		99

Superscripts denote: (*) due to small sample size, 1B 144.04 m gouge was not sieved to <150 μm; ([a]) the smectite mineral present is dioctahedral smectite (montmorillonite); ([b]) the smectite mineral present is trioctahedral smectite (saponite); ([c]) the serpentine mineral present is lizardite. Trace amounts of anatase and pyrite were found in samples 1A 90.62 m and 1B 144.04 m, respectively. WR refers to whole rock; <2 μm refers to the clay-sized fraction.

denote the slip-weakening distance in high-velocity experiments (Niemeijer et al., 2012). In fitting Equation (2), values of μ_p and μ_{ss} were fixed manually, displacement was zeroed at μ_p, and d_w was determined using a least-squares method.

Quantifying energy partitioning during high-velocity friction experiments, conducted at coseismic rates of >0.1 m/s, may allow extrapolation of laboratory results to natural seismogenic faults (e.g., Beeler, 2006; Niemeijer et al., 2012). To that end, many researchers have correlated the integral of shear stress-displacement curves in high-velocity experiments with seismological breakdown work, the work done at a point on a fault to propagate an earthquake rupture (e.g., Cocco and Tinti, 2008; Niemeijer et al., 2012). In this study, the term specific fracture energy (E_G) is adopted following Togo et al. (2011) and Yao et al. (2013a). Specific fracture energy (E_G), in units of MJ/m^2, was calculated by multiplying the integral of the raw friction data by normal stress (1 MPa) (e.g., Fig. 3). Since specific fracture energy was calculated from raw data, the value reported in Table 2 includes a small amount attributable to Teflon® (c. 0.01 MJ/m^2). Specific fracture energy does not include frictional work done below μ_{ss} (Cocco and Tinti, 2008).

4. High-velocity friction results

4.1. Room-dry high-velocity friction experiments

In all eleven room-dry (dry) experiments, central and southern Alpine Fault foliated cataclasite, cataclasite, and gouge powders exhibited a pronounced (>2.6-fold) reduction in the coefficients of friction from peak values ($\mu_p = 0.53$–0.78; mean $\mu_p = 0.67 \pm 0.07$) to steady-state values ($\mu_{ss} = 0.06$–0.25; mean $\mu_{ss} = 0.16 \pm 0.05$). Slip-weakening distances (d_w) necessary to achieve steady-state friction ranged from 3.54 m to 8.34 m, with a mean of 5.14 ± 1.60 m (Fig. 4a,c and 5a) (Table 2). In the high-velocity friction experiment with decelerating slip, LHV583, restrengthening occurred during the final 1 m of displacement, resulting in a final friction coefficient ($\mu_f = 0.32$) higher than the steady-state friction coefficient ($\mu_{ss} = 0.17$) (Fig. 5a). In the high-velocity friction experiment with afterslip, LHV581, the peak friction coefficient ($\mu_p = 0.80$) at $v_{eq} = 0.001$ m/s was higher than peak friction coefficient ($\mu_p = 0.61$) recorded at $v_{eq} = 1$ m/s (Fig. 5a). In the dry experiments, peak friction was coincident with a dramatic decrease in gouge thickness, followed by dilation, and finally near-constant

Table 2
Summary of high-velocity friction experiments and results.

Experiment	Material	Lithology	Dry/Wet	σ_n (MPa)	v_{eq} (m/s)	d_{eq} (m)	$\mu_{p\ corrected}$	$\mu_{ss\ corrected}$	d_w (m)	E_G (MJ/m^2)
LHV281	1A 86.41 m	4	Dry	1.0	1.0	20.54	0.74	0.21	5.16	0.88
LHV284	1A 86.41 m	4	Wet	1.0	1.0	20.96	0.59	0.11	6.78	0.98
LHV282	1A 90.32 m	4	Dry	1.0	1.0	20.77	0.65	0.25	6.37	0.79
LHV285	1A 90.32 m	4	Wet	1.0	1.0	20.85	0.65	0.13	4.81	0.75
LHV279	1A 90.62 m	5	Dry	1.0	1.0	20.00	0.68	0.19	8.34	1.37
LHV286	1A 90.62 m	5	Wet	1.0	1.0	20.80	0.47	0.12	0.23	0.02
LHV277	GC Scarp PSZ	5	Dry	1.0	1.0	21.37	0.78	0.18	5.34	0.97
LHV278	GC Scarp PSZ	5	Wet	1.0	1.0	20.17	0.14	0.06	15.56	0.39
LHV574	1B 128.44 m	5	Dry	1.0	1.0	20.00	0.53	0.14	3.58	0.43
LHV579	1B 128.44 m	5	Wet	1.0	1.0	20.30	0.17	0.09	20.90	0.45
LHV583[a]	1B 128.44 m	5	Dry	1.0	1.0	20.03	0.58	0.17	3.76	0.45
LHV584[a]	1B 128.44 m	5	Wet	1.0	1.0	20.12	0.20	0.07	17.96	0.69
LHV581	1B 128.44 m	5	Dry	1.0	1.0, 0.001	22.13	0.61	0.06	5.44	0.97
LHV582	1B 128.44 m	5	Wet	1.0	1.0, 0.001	21.93	0.10	0.07	9.00	0.08
LHV280	1B 128.80 m	6	Dry	1.0	1.0	17.70	0.67	0.18	7.09	1.12
LHV287	1B 128.80 m	6	Wet	1.0	1.0	20.62	0.67	0.14	0.75	0.12
LHV283	1B 144.04 m	5	Dry	1.0	1.0	20.58	0.68	0.15	4.37	0.73
LHV288	1B 144.04 m	5	Wet	1.0	1.0	20.24	0.18	0.09	27.77	0.68
LHV262[b]	HkC PSZ	5	Dry	1.0	1.0	15.20	0.73	0.14	3.54	0.63
LHV272	HkC PSZ	5	Dry	1.0	1.0	16.25	0.71	0.13	3.57	0.62
LHV289	HkC PSZ	5	Wet	1.0	1.0	20.17	0.16	0.03	0.25	0.01

Symbols are: (σ_n), normal stress in MPa; (v_{eq}) equivalent slip velocity in m/s; (d_{eq}) total equivalent slip distance in m; (μ_p) peak coefficient of friction; (μ_{ss}) steady state coefficient of friction; (d_w) total slip-weakening distance in m; (E_G) specific fracture energy in MJ/m^2 calculated as the integral of the raw friction data multiplied by the applied normal stress. d_{eq} was calculated as the product of total time and v_{eq}. ([a]) Experiments LHV583 and LHV584 are high-velocity friction experiments with decelerating slip ([b]) LHV262 was pre-compacted at 2 MPa normal stress.

thickness during shearing at steady-state friction coefficients (Fig. 5b).

4.2. Wet high-velocity friction experiments

Relative to the dry experiments conducted on the same materials, ten wet experiments on central and southern Alpine Fault foliated cataclasite, cataclasite, and gouge powders exhibited a wider range of peak friction coefficients (μ_p = 0.10–0.67; mean μ_p = 0.33 ± 0.23) and steady-state friction coefficients (μ_{ss} = 0.03–0.14; mean μ_{ss} = 0.09 ± 0.04) values. Fitting Equation (2) to the wet high-velocity data resulted in a considerable range of slip-weakening distances due to the deviation from clear exponential decay-type behaviors exhibited by the smectitic PSZ gouges. Slip weakening distances (d_w) varied from 0.25 m to 27.77 m with a mean of 10.401 ± 9.67 m (Figs. 4b, d and 5c) (Table 2). As shown in Fig. 6a, experiments on wet smectitic materials exhibited the lowest values of steady-state friction and peak friction measured in the suite of HVFEs performed (Table 2).

In the HVFE with decelerating slip, LHV584, restrengthening occurred during the final 1 m of displacement, resulting in a final friction coefficient (μ_f = 0.10) slightly higher than the steady-state friction coefficient (μ_{ss} = 0.07) (Fig. 5c). In the HVFE with afterslip, LHV 582, the peak friction coefficient (μ_p = 0.28) during sliding at v_{eq} = 0.001 mm/s was higher than peak friction (μ_p = 0.10) recorded at v_{eq} = 1 m/s (Fig. 5c). Wet samples exhibited smaller amounts of compaction compared to dry samples (Fig. 5d). Displacement at near steady-state friction coefficients was coincident with increases in gouge thickness indicative of dilation. Compaction occurred towards the end of each experiment and during low-velocity sliding in LHV582 (Fig. 5d). Since Teflon® sleeves are not perfect seals, some compaction may be related to the escape of fluid or fluid-gouge mixtures.

4.3. Specific fracture energy in dry and wet high-velocity friction experiments

Relative to dry experiments conducted on the same materials (mean E_G = 0.81 ± 0.28 MJ/m^2), lower values of specific fracture energy are commonly associated with wet high-velocity friction experiments (mean E_G = 0.42 ± 0.35 MJ/m^2) (Fig. 6b). The foliated cataclasites from 1A 86.41 m and 1A 90.32 m, and the 1B 144.04 m PSZ-2 gouge, exhibited similar specific fracture energy values for dry and wet experiments (Table 2). The small differences in E_G between dry and wet experiments reflect both material properties and errors in the slip-weakening distance values. For wet experiments on the smectitic gouges, the very low gradients in friction coefficient introduce large uncertainties in the determination of slip-weakening distance using equation (2), and thus large (positive) errors in specific fracture energy (Figs. 3, 4d and 5c).

5. Temperature changes during the high-velocity friction experiments

5.1. Finite element model methods

Shear heating strongly influences frictional strength, but temperatures within the slip zones were not measured during the high-velocity friction experiments (e.g., Di Toro et al., 2011; Yao et al., 2016). Instead, temperature changes were modeled using COMSOL Multiphysics finite element software. Thermomechanical modeling was performed following procedures similar to those outlined by Kitajima et al. (2010), Han et al. (2011), and Yao et al. (2013b). The 2-D axisymmetric geometric model used in the calculation was constructed using a replica of the sample assembly replete with host blocks, Teflon® sleeve, and 1.2 mm-thick gouge layer (Fig. 7a).

In the model, the primary heat source was the measured friction acting along a planar boundary between the fault rock sample and rotating wall rock, assuming all frictional work was converted to heat. The friction along the Teflon sleeve/rotating host rock interface was set as a secondary heat source (Fig. 7a). Energy consumed by dehydration/dehydroxylation reactions in smectite and/or illite was ignored in the model, but the enthalpy of these reactions is only a few percent of the frictional work in

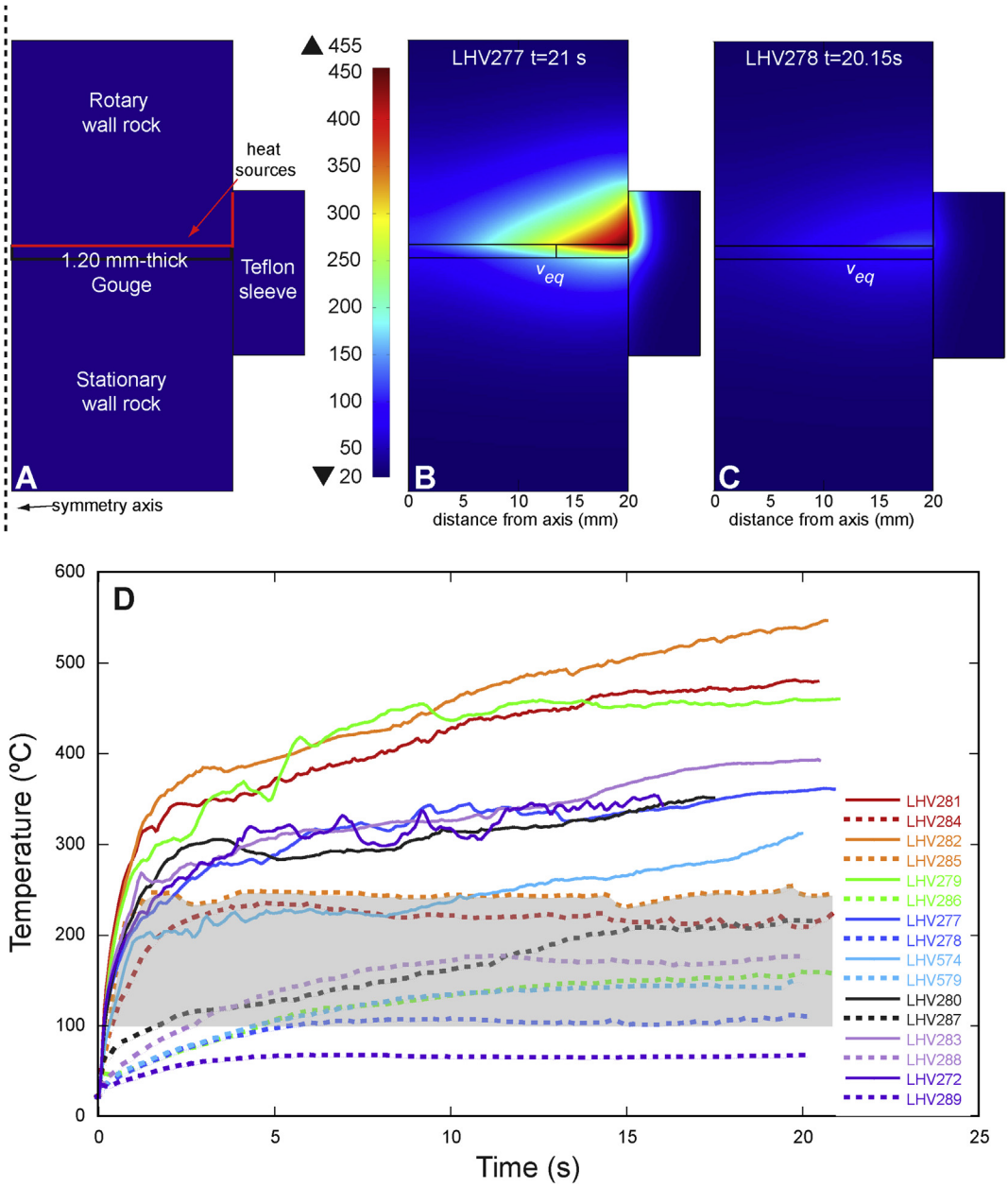

Fig. 7. Results from thermomechanical temperature modeling of experiments performed on Alpine Fault rocks. (a) Geometry of the COMSOL software model based on the experimental configuration. Horizontal scale is given as distance from the axis of symmetry. The model gouge layer is 1.2 mm-thick and serves as the vertical scale. (b, c) Maximum temperature reached in the outer half of GC PSZ Scarp gouge samples deformed dry and wet, respectively. (d) Maximum temperature in each sample plotted against total time elapsed since the start of each LHV experiment. Where gouge temperatures exceeded 100 °C in the wet experiments, model results yield only estimates of the maximum temperature reached (shaded region). Models were constructed for experiments: LHV281 and LHV 284 (1A 86.41 m foliated cataclasite); LHV282 and LHV 285 (1A 90.32 m foliated cataclasite); LHV279 and LHV286 (1A 90.62 m gouge); LHV 277 and LHV278 (GC Scarp PSZ gouge); LHV574 and LHV579 (1B 128.44 m gouge); LHV280 and LHV287 (1B 128.80 m lower cataclasite); LHV283 and LHV288 (1B 144.04 m gouge); and LHV272 and LHV289 (HkC PSZ gouge).

high-velocity friction experiments (Kitajima et al., 2010; Hirono et al., 2013; see also French et al., 2014). Temperature changes were calculated by solving a simple transient heat problem with the temperature at the upper and lower surfaces of the model assumed to be 25 °C and the temperature of the surfaces exposed to air allowed to evolve following Newton's cooling law. A table of the thermal properties used in the temperature calculations, including thermal conductivity, specific heat, density, and porosity of the fault gouges, can be found in Supplementary material (Table S1).

5.2. Modeled temperature changes

For solid cylindrical shear zones, 87.5% of experimentally measured torque is exerted by friction in the outer half of the experimental gouge zones if a spatially uniform friction coefficient is assumed (Fig. 7b and c) (Yao et al., 2013b). Since the high-velocity friction data primarily reflect processes occurring on the outer half of the cylindrical shear zones, the maximum temperature change and average temperature change in these regions were calculated. For dry and wet experiments, the average temperature changes are

approximately 77–80% and 89–91% of the modeled maximum temperature change, respectively.

Maximum temperature changes are plotted in Fig. 7. All dry fault rocks exhibited a sharp, linear increase in temperature during the slip-weakening phase, reaching maximum temperatures exceeding 200 °C prior to attaining steady-state friction coefficients. Maximum temperatures continued to rise gradually during steady-state sliding, reaching values of 404–480 °C by the end of the experiments. In the dry HVFEs, there was no correlation between total temperature rise and mineralogy or phyllosilicate content. Maximum temperatures in the wet HVFEs increased more gradually. Although the phyllosilicate-rich (non-smectitic) 1A 90.32 m gouge attained a maximum temperature of 252 °C, the maximum temperature rise in wet smectitic fault gouges was limited to ≤176 °C (Fig. 7d). The models likely overestimate maximum temperatures in the wet HVFEs because they do not account for the latent heat associated with the pore fluid liquid-vapor transition (e.g., Brantut et al., 2011; Chen et al., 2017) (shaded region of Fig. 7d).

6. Microstructures produced during high-velocity experiments

6.1. Methods and observational framework

This microstructural analysis focuses on the LHV500-series experiments (Table 2). Following each experiment, deformed fault rock and host rock samples were impregnated with LR White resin, a low-viscosity epoxy resin, and vacuum dried overnight at 60 °C. Thin sections of microstructures produced were cut radially through the axis of the sample cylinder, prepared dry, and polished using 1 μm diamond paste (inset Fig. 3). Microstructures were imaged using a standard optical microscrope (OM) and Philips XL30 tungsten filament scanning electron microscope (SEM) with a backscatter electron (BSE) and energy dispersive spectroscopy (EDS) detectors, 20 kV accelerating voltage and 13 mm working distance.

Microstructures observed in radially cut thin sections through cylindrical shear zones formed at velocities that range from $v = 0$ m/s at the axis of rotation to $v = 1.50$ m/s at a radial distance of 20 mm (e.g., Kitajima et al., 2010; French et al., 2014). Variations in rotational velocity cause commensurate changes in temperature and shear strain (Figs. 7 and 8). Therefore, detailed analysis focuses on 1B 128.44 m PSZ-1 gouge microstructures formed at a radial distance of 12–15 mm and an equivalent slip velocity (v_{eq}) of c. 1 m/s; how simulated afterslip affects these microstructures is also discussed (Figs. 9–12). Composite images for all microstructures produced in dry and wet high-velocity experiments on the 1A 90.32 m foliated cataclasite, 1A 90.62 m gouge, GC Scarp PSZ, and 1B 128.44 m gouge are located in the Supplementary material (Fig. S1).

6.2. Microstructure descriptions

Microstructures formed during the dry high-velocity experiments on the 1B 128.44 m gouge are characterized by grain size reduction, porosity reduction, and particle rounding, i.e., cataclastic flow processes (Sibson, 1977; Borradaile, 1981). A coarse-grained low-strain gouge containing subrounded to rounded clasts of the initial granular material forms the majority of the sample at the axis of rotation (Fig. 8a,c and e). Grain size decreases with distance from the axis of rotation and with proximity to the rotating wall rock (Figs. 8g, 9a,c and e).

Two sets of microshears inclined symmetrical to the axis of rotation separate the low-strain gouge from a very fine-grained gouge containing subangular to well-rounded mineral and lithic grains and clay-clast aggregates (CCAs). CCAs were defined by Boutareaud et al. (2008, 2010) as central mineral or aggregate grains surrounded by a cortex of concentric clay layers commonly including very fine (<5 μm) mineral fragments (Figs. 9a,c,e and 10). Whereas most central grains are pristine, some potassium feldspar and calcite grains are highly pitted, suggesting chemical disequilibrium (Fig. 10e and f). The original Alpine Fault PSZ gouges contain similar grains; thus, it is not possible to discern whether natural and/or experimental processes are responsible for producing the disequilibrium conditions.

The highest-strain, finest-grained gouge forms microfoliated layers composed of individual elongated grains; these layers appear light brown in plane-polarized light (e.g., Fig. 8g). The microfoliated gouge ranges in thickness from <1 μm to c. 200 μm and occurs along the boundary of the rotating wall rock, interbedded with the CCA-bearing gouge, and/or between the CCA-bearing gouge and the low-strain gouge (Figs. 8a,c,e, 9a,c,e and 10). Element maps, complemented by semi-quantitative EDS analyses, illustrate that the microfoliated gouge has more iron, magnesium, and aluminium, and less calcium and silica, than the other two gouge units described (Fig. 10b,d and f). The microfoliated gouge shares chemical and particle-size affinities with material surrounding the CCAs (Fig. 10).

A distinguishing characteristic of the microfoliated gouge is the presence of a strongly developed phyllosilicate foliation, which is observable in an optical microscope when viewed with both polarizers and the full lambda retardation plate inserted. The microfoliated gouge appears strongly orange/yellow or blue/purple at different rotations with respect to polarizers and the lambda plate, indicating it has a moderately strong crystallographic preferred orientation (CPO). With a full-lambda retarding plate inserted, the matrix of the CCA-bearing gouge appears opaque, and clays within the low-strain gouge display no distinct colour variation; thus these have no CPO (Fig. 12a and b). There is no observable difference between microstructures formed during the three dry experiments (Figs. 8–10).

The 1B 128.44 m gouges deformed in wet high-velocity friction experiments were scarcely affected by particle rounding and grain-size reduction processes, and they appear uniformly brown in plane-polarized light images. Microstructurally, the smectitic gouge forms thick packages of matrix-supported grains that display little variation with increasing distance from the axis of rotation (Fig. 8). Two distinct microstructures occur together at radial distances between ~5 and ~17 mm: a layer of reverse-graded (fine-to-coarse-grained) gouge adjacent to the lower, stationary wall rock, and a thin (≤0.20 mm-thick) gouge containing phyllosilicate lamellae with a crystallographic preferred orientation adjacent to the upper (rotating) wall rock (Figs. 1,9,11 and 12d).

In the wet HVFE with afterslip, the thin layer of aligned phyllosilicate lamellae was preserved. However, clasts within the reverse-graded layer appear to have been redistributed, and a foliation defined by crystallographically aligned phyllosilicates formed oblique to the wall rock contact at radial distances between ~5 and ~10 mm (Fig. 11e and f). In the wet experimental microstructures, element maps and semi-quantitative EDS analyses show no compositional differences between the layers (Fig. 11b,d and f). Small- and large-scale cracks with a quasi-hexagonal appearance indicative of shrinkage cracks overprint all syn-deformational microstructures formed in the wet experiments (Fig. 8).

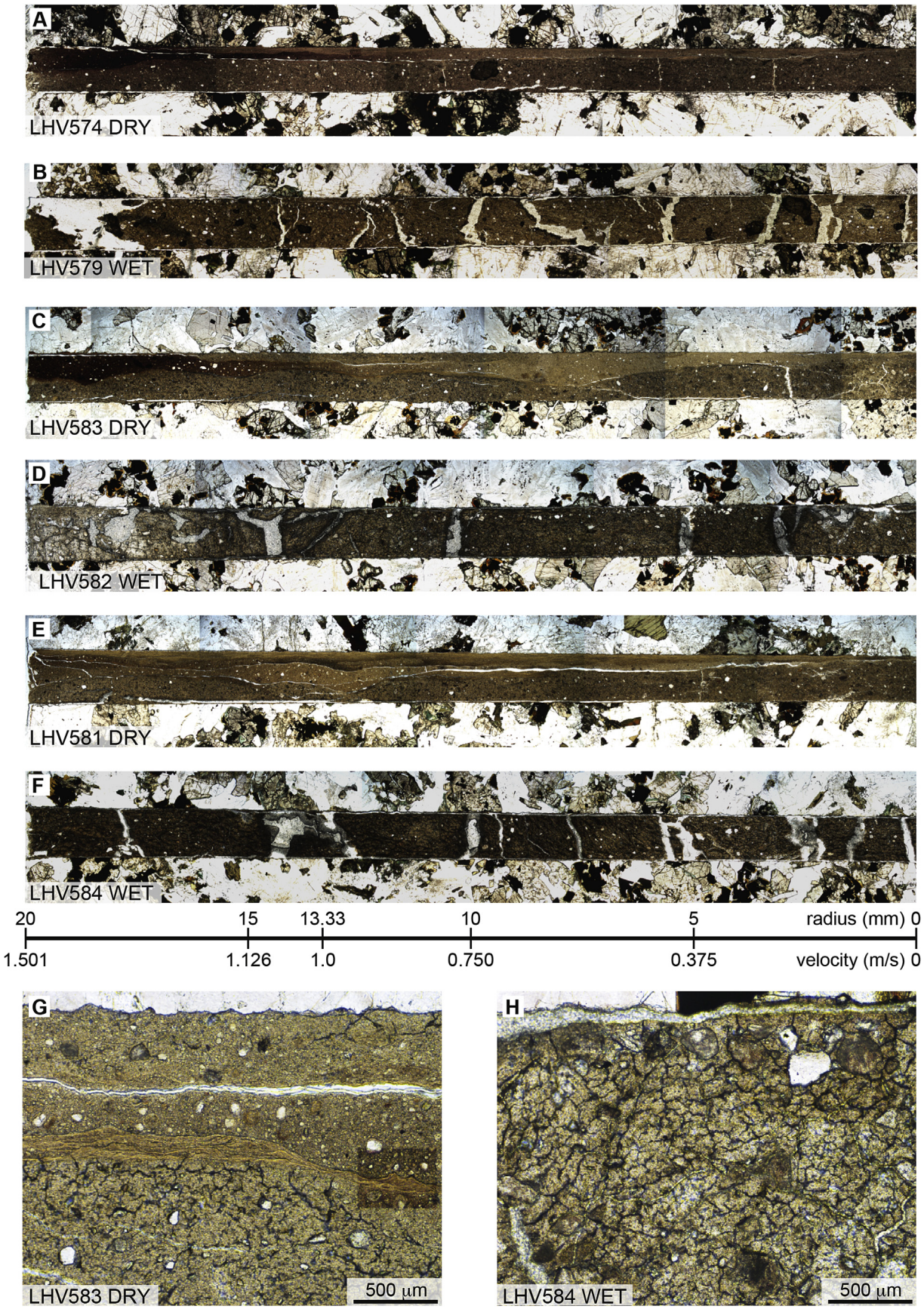

Fig. 8. (a–f) Composite plane-polarized light (PPL) optical microscope images of microstructures exposed in radially cut thin sections prepared following the high-velocity friction experiments with different velocity histories. The scale beneath the images is given as radial distance, in mm, from the axis of symmetry. Equivalent slip velocity, in ms^{-1}, is also given. (g,h) PPL image of gouge units formed in the dry and wet high-velocity friction experiments with decelerating slip, respectively. In all images, the rotary wall rock is above the gouge. See text for details.

7. Discussion

7.1. Yield strength during high-velocity friction experiments

Earthquake nucleation occurs at very low sliding velocities (Marone, 1998; Scholz, 1998, 2002). Once an earthquake nucleates, acceleration to coseismic slip rates at a rupture front may result in a peak friction (equal to τ_p/σ_n') that differs from the steady state coefficient of friction measured in low-velocity sliding experiments (e.g., Beeler, 2006; see also Ben-Zion, 2008). Quantifying the effect that acceleration to coseismic slip rates (e.g., v~1 m/s) might have on the peak coefficient of friction is important because this gives insight into the yield strength and barrier to rupture propagation, although these parameters are likely to depend on the specific velocity evolution during an earthquake (see also Section 7.4). On average, all wet experiments conducted had lower values of peak friction (mean $\mu_p = 0.33 \pm 0.23$) compared to the dry experiments on the same material (mean $\mu_p = 0.67 \pm 0.07$) (Table 2) (Fig. 6a).

The wet smectite-bearing fault gouges, GC Scarp PSZ, 1B 128.44 m, 1B 144.04 m, and HcK PSZ, were the only gouges to exhibit extremely low values of peak friction ($\mu_p = 0.10–0.20$), consistent with previous HVFE studies that show as little as 10 wt% montmorillonite can suppress peak friction in simulated gouge mixtures (Bullock et al., 2015). The peak friction coefficients obtained from smectitic Alpine Fault gouges are also consistent with results from wet high-velocity ($v_{eq} = 1.3$ m/s) friction experiments on smectitic Vaiont landslide gouge conducted at the same normal stress ($\mu_p = 0.10–0.19$) (Ferri et al., 2011). The extremely low yield strength of the wet Alpine Fault smectitic gouges would make earthquake rupture propagation through these materials energetically favorable (Faulkner et al., 2011; Oohashi et al., 2015; Remitti et al., 2015). Indeed, the high-velocity frictional behavior of Alpine Fault PSZ gouges lends credence to the interpretation of multiple episodes of slip in Alpine Fault PSZ gouges from microstructural observations of reworked smectite-bearing gouge clasts (e.g., Fig. 2b) (Boulton et al., 2012, 2017; Toy et al., 2015a).

7.2. Evolution of friction during high-velocity sliding

In the dry high-velocity experiments, evolution of fault strength to steady-state values followed an exponential decay function similar to velocity steps in low-velocity friction experiments. However, there are three important differences: (1) all materials are slip-weakening at coseismic slip rates $v = 1$ m/s, even smectite-bearing fault gouges that were velocity-strengthening in low-velocity ($v = 0.01–300$ μm/s) room-temperature experiments (Boulton et al., 2012, 2014; Barth et al., 2013; Ikari et al., 2014) (2) weakening following smaller-magnitude velocity perturbations in low-velocity friction experiments occurs over at least 5 orders of magnitude smaller distances than that observed in the high-velocity experiments (mean $d_w = 5.14 \pm 1.60$ m; n = 11), and (3) the weakening is about an order of magnitude greater in high-velocity experiments (mean $\Delta\mu = 0.51 \pm 0.08$; n = 11) (Table 2; Figs. 4 and 6).

During small-displacement ($d < 20$ mm), low sliding velocity ($v \leq 200$ μm/s) experiments, measured changes in temperature for gouges materials are small ($\Delta T \leq 2.5$ °C), the degree of mechanical wear is typically low, the critical slip distance (d_c) needed to renew a population of contacts is short ($d_c < 100$ μm), and the corresponding change in the coefficient of friction is relatively small ($\Delta\mu < 0.03$) (Fulton and Rathbun, 2011; Marone, 1998; Noda and Shimamoto, 2009; Boulton et al., 2014). At high sliding velocity ($v \geq 1$ m/s) and large displacement ($d > 0.1$ m), rapid comminution and frictional heating ($\Delta T \approx 100–900$ °C) in granular materials result in complex rate-dependent thermomechanical and possibly thermochemical processes (Sone and Shimamoto, 2009; Boutareaud et al., 2008, 2010; Kitajima et al., 2010; Di Toro et al., 2011; Niemeijer et al., 2012; Platt et al., 2015; French et al., 2014; Yao et al., 2016) (cf., Fig. 7). These processes result in strong slip weakening in high-velocity experiments.

7.3. Potential weakening mechanisms

All Alpine Fault rocks deformed in the dry high-velocity friction experiments underwent grain size reduction and particle rounding along the upper gouge/wall rock contact (cf., Fig. 9). Although potential dynamic weakening mechanisms in comminuting granular materials include silica gel or powder lubrication (Goldsby and Tullis, 2002; Di Toro et al., 2004; Reches and Lockner, 2010; Han et al., 2010), recent microstructural and experimental studies indicate that nanoparticles (with grain size less than 100 nm) alone are insufficient for dynamic weakening (Yao et al., 2016). Alternatively, flash heating at highly stressed frictional micro-contacts may have occurred (Rice, 2006; Beeler et al., 2008; Noda et al., 2009; Goldsby and Tullis, 2011; Yao et al., 2016). Flash heating induces weakening by catalyzing phase changes at the micro-contacts (sometimes called “thermal softening”).

For slip along a bare-rock slip surface, slip weakening due to flash heating is predicted to occur over distances comparable to the maximum micro-contact size (e.g., a few tens of micrometers). This theoretically predicted slip-weakening distance is orders of magnitude smaller than that recorded in the dry experiments (Table 2). Extrapolating results from numerical models of flash heating to gouge-filled shear zones remains difficult because of a number of poorly quantified variables that evolve with displacement (e.g., contact dimension, thermal diffusivity, volumetric heat capacity) (Beeler et al., 2008). However, results from recent high-velocity gouge experiments indicate that flash heating can initiate slip weakening in granular materials due to (1) a rise in the bulk temperature of the material and/or (2) deformation localization onto a narrow slip surface(s) (Nielsen et al., 2013; Platt et al., 2014). Both processes increase local temperature, which in turn decreases the critical velocity required to activate flash-weakening in gouges, albeit over larger length scales than those predicted for bare-rock surfaces (e.g., Proctor et al., 2014; Yao et al., 2016; see also Passelègue et al., 2014).

In addition to experiencing flash heating at grain contacts, average temperatures required to dehydrate smectite ($T = 140–280$ °C at $\sigma_n = 0–1$ MPa) and/or vaporize water ($T = \sim 180$ °C at $\sigma_n = 0.6–1$ MPa) were reached in the HVFEs on dry smectitic PSZ gouges (Koster van Groos and Guggenheim, 1984; Lide, 2008; Hirono et al., 2013) (Fig. 7). Thus, in the later stages of the dry experiments, PSZ gouges may have experienced smectite dehydration accompanied by pressurization and vaporization of the released fluids (Fig. 7) (e.g., Ujiie and Tsutsumi, 2010; Faulkner et al., 2011; Oohashi et al., 2015; Remitti et al., 2015; French et al., 2014). This water vapor could only have created an internal pressure if it did not escape past the Teflon® sleeve (De Paola et al., 2011; Chen et al., 2013).

In the wet high-velocity friction experiments, peak friction values were lower than those recorded in the dry experiments; in addition, μ_p occurred contemporaneously with either dilation or a smaller amount of compaction, and μ_{ss} was accompanied by an increase in gouge thickness (i.e., dilation) (Fig. 5). Thermomechanical models indicate that temperature increases within fault rocks deformed wet were insufficient to cause dehydration and vaporization of structurally bound water (cf. Kitajima et al., 2010) (Fig. 7). Therefore, a separate dynamic weakening mechanism(s) must have operated in the saturated gouges. In shallow crustal fault zones comprising fluid-saturated granular material,

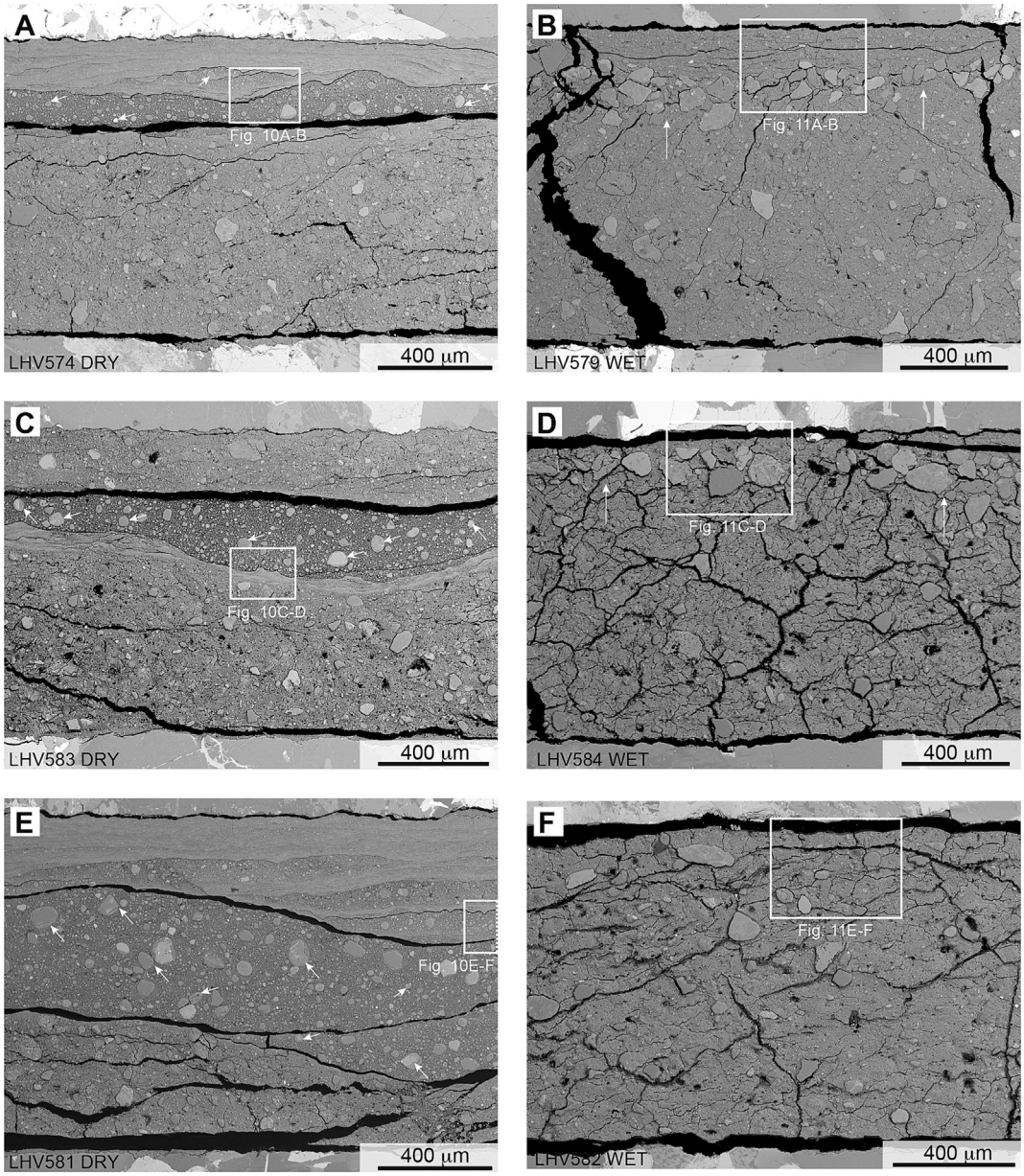

Fig. 9. Backscattered electron (BSE) images of microstructures formed at v_{eq}~1 ms^{-1} in the high-velocity friction experiments with different velocity histories. White boxes denote the location of images in subsequent figures. The upper wall rock is at the top of all images. (a,b) BSE images of microstructures formed in dry (LHV574) and wet (LHV579) constant velocity experiments, respectively. (c,d) BSE images of microstructures formed in dry (LHV583) and wet (LHV584) HVFE with decelerating slip, respectively. (e,f) BSE images of microstructures formed in dry (LHV581) and wet (LHV582) HVFE with afterslip, respectively. Arrows in all dry experiments indicate the location of prominent CCAs. Arrows in wet experiments LHV579 and LHV584 show the location of large clasts at the top of the reverse-graded gouge. See text for details.

thermal pressurization of pore fluid is widely considered to be the dominant weakening mechanism at slip rates greater than c. 0.1 m/s (e.g., Sibson, 1973; Lachenbruch, 1980; Andrews, 2002; Wibberley and Shimamoto, 2005; Bizarri and Cocco, 2000a,b; Rice, 2006; Noda et al., 2009; Schmitt et al., 2011; Garagash, 2012). Thermal pressurization occurs because the thermal expansion of pore fluid is greater than the thermal expansion of pore space. Thus, pore-fluid pressure increases with cumulative slip unless fluid diffusion and/or dilatancy dissipate the pressure increase (e.g., Garagash and Rudnicki, 2003; Rice, 2006; Segall et al., 2010). During rapid coseismic slip, the rate of frictional heating is thought to greatly exceed the rate of fluid diffusion, and localized slip surfaces less than ~1 mm-thick can undergo undrained adiabatic shearing (e.g., Lachenbruch, 1980; Wibberley and Shimamoto, 2005; Rice, 2006; Garagash and Germanovitch, 2012).

Lachenbruch (1980) identified the material properties requisite for thermal pressurization to occur, namely: the heat production rate, which is governed by frictional heat generation, bulk density, specific heat, thermal conductivity, and deformation zone width; and the rate of pore-pressure change, which is governed by water expansibility, specific storage, permeability, porosity, fluid density, fluid viscosity, and deformation zone width (see also Wibberley and Shimamoto, 2005; Tanikawa and Shimamoto, 2009). In lieu of quantifying the thermal and hydraulic transport properties of all Alpine Fault materials tested, and how these properties change with effective pressure and displacement at coseismic slip rates, the theoretical considerations proposed by Andrews (2002) and Mizoguchi (2005) suggest that materials with a permeability of

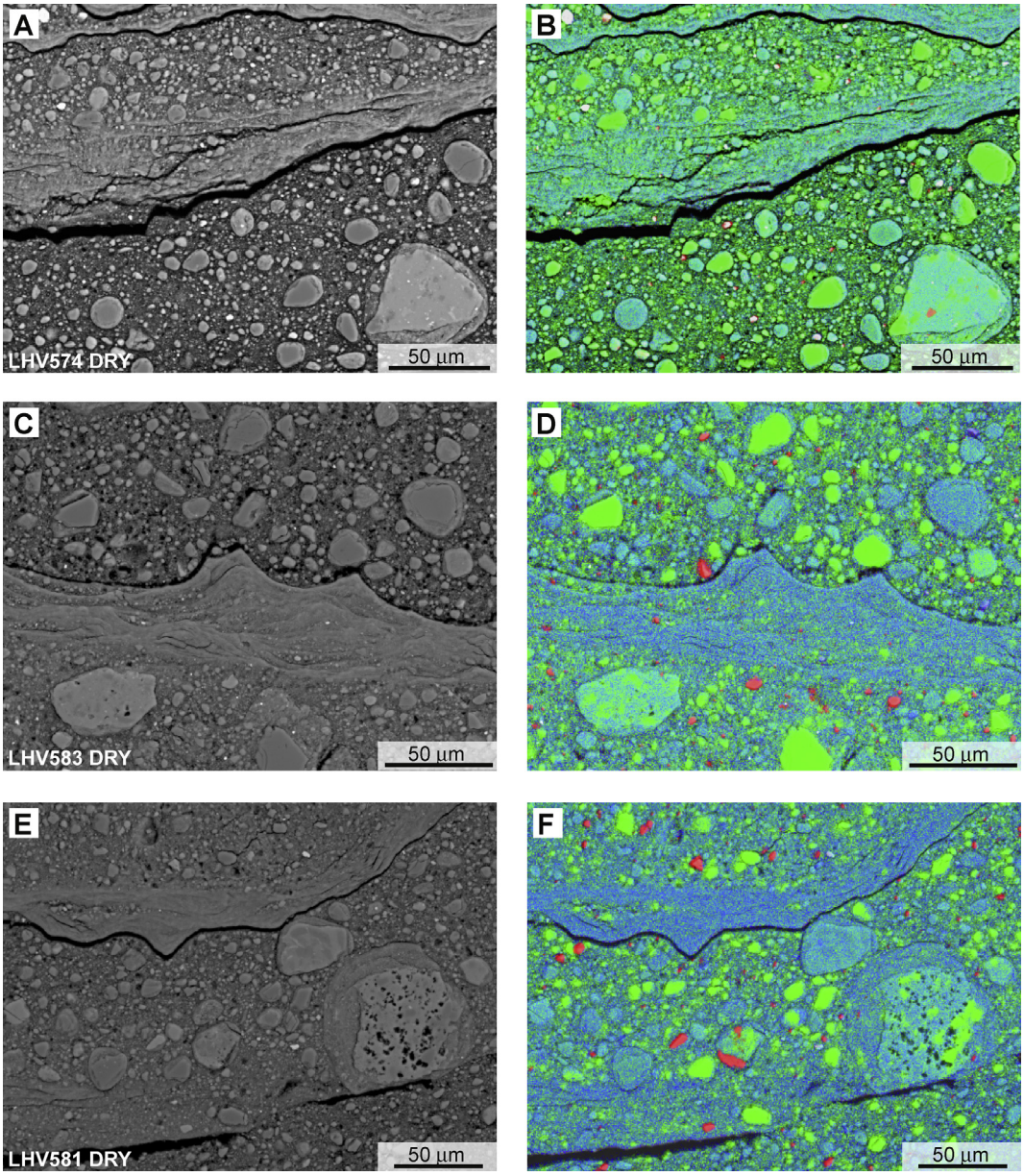

Fig. 10. Backscattered electron (BSE) images and energy dispersive spectroscopy (EDS) maps of microstructures formed at v_{eq}~1 ms^{-1} in the dry HVFEs with different velocity histories. In all EDS maps, red denotes calcium, green denotes silica, and blue denotes aluminum. (a,b) BSE image and EDS map of the ultrafine-grained microfoliated gouge and CCA-bearing gouge formed in the dry constant velocity experiments, LHV574. Whereas most central CCA clasts are well-rounded, the large CCA with a pitted K-feldspar core in the lower right corner is angular. (c,d) BSE image and EDS map of the CCA-bearing gouge (top), ultrafine-grained microfoliated gouge (center) and low-strain gouge formed (bottom) in the dry HVFE with decelerating slip, LHV583. (e,f) BSE image and EDS map of interbedded ultrafine-grained microfoliated and CCA-bearing gouges formed in the dry HVFE with afterslip, LHV581. See text for further details. (For interpretation of the references to colour in this figure legend, the reader is referred to the web version of this article.)

$k = 10^{-17}$ m^2 or less are likely to undergo thermal pressurization during high velocity shearing on a localized slip surface. Thermal pressurization also requires low permeability wall rocks ($k = 10^{-16}$ m^2) (Tanikawa and Shimamoto, 2009; Ujiie et al., 2013). Although the gabbro wall rocks used were effectively impermeable on the timescale of the experiments ($k < 10^{-22}$ m^2), water on the outside of the sample assembly after each wet test indicates that the Teflon® sleeves had a poor sealing capacity.

The permeability of surface outcrop PSZ gouges at Gaunt Creek is on the order of $k = 10^{-20}$ m^2, with hanging-wall cataclasites having higher permeabilities, $k = 10^{-18}$ m^2 to 10^{-16} m^2 (confining pressure (P_c)=30–31 MPa) (Boulton et al., 2012). Over a wide range of pressures (P_c = 2.5–63.5 MPa), Carpenter et al. (2014) measured the permeabilities of DFDP-1A hanging wall cataclasites ($k = 10^{-15}$–10^{-18} m^2) and DFDP-1B gouge ($k = 10^{-19}$–10^{-20} m^2). A DFDP-1B footwall cataclasite was slightly more permeable ($k = 10^{-16}$–10^{-17} m^2). The HkC PSZ gouge permeability was $k = 10^{-21}$ m^2 (P_c = 30 MPa) (Barth et al., 2013). All permeability measurements were made on static materials; high-velocity sliding has been shown to decrease further the permeability of deformed specimens (Tanikawa et al., 2012). These permeability measurements indicate that thermal pressurization may have occurred in any of the fault rocks tested, although probably not at low confining pressures in the HVFEs on hanging-wall and footwall cataclasites

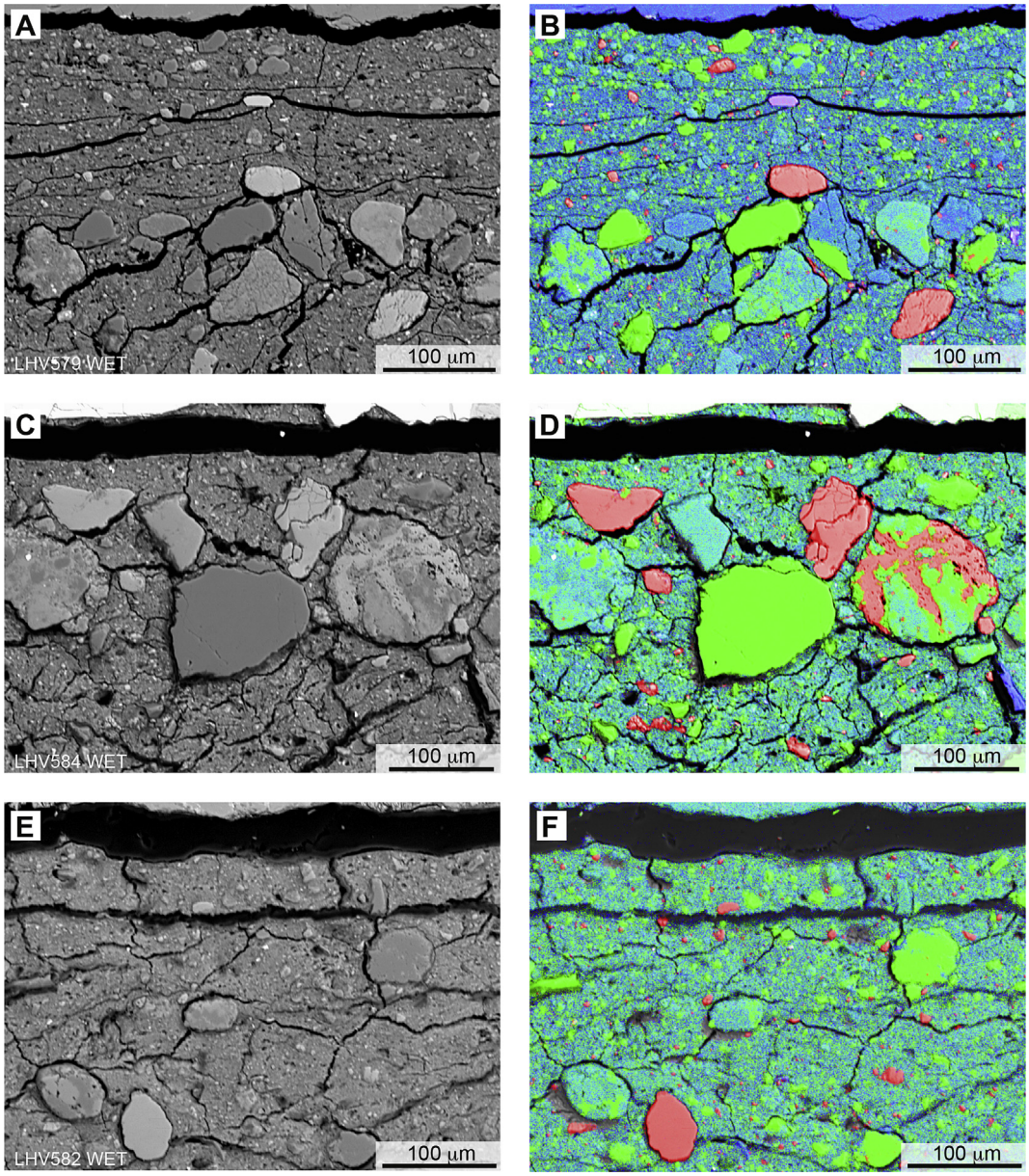

Fig. 11. Backscattered electron (BSE) images and energy dispersive spectroscopy (EDS) maps of microstructures formed at v_{eq}~1 ms^{-1} in the wet HVFEs with different velocity histories. In all EDS maps, red denotes calcium, green denotes silica, and blue denotes aluminum. (a,b) BSE image and EDS map of the reverse-graded and laminar layers formed in the wet constant velocity experiments, LHV579. Note the weak shape-preferred orientation in the laminar layer. (c,d) BSE image and EDS map of the reverse-graded and laminar layers formed in the wet HVFE with decelerating slip, LHV584. Note the strongly pitted fracture-filling calcite in the right-hand clast; this texture occurs in calcite within natural Alpine Fault gouges. (e,f) BSE image and EDS map of the gouges formed in the wet HVFE with afterslip, LHV582. Clasts within the reverse-graded layer have mixed with matrix grains, and the boundary between the two layers is gradational. See text for further details. (For interpretation of the references to colour in this figure legend, the reader is referred to the web version of this article.)

(compare wet slip-weakening curves in Figs. 4 and 5).

Quantifying pore-fluid pressure during high-velocity friction experiments remains an ongoing challenge in experimental rock mechanics (e.g., Violay et al., 2015). In the absence of pore-fluid pressure measurements, data from experiments conducted at the same velocity under a wide range of normal stresses, combined with microstructural analyses are required to help identify the processes responsible for the evolution of frictional strength recorded in each Alpine Fault rock; this is beyond the scope of this research. Instead, the focus is placed on relating mechanical data with microstructures obtained from the high-velocity friction experiments conducted on 1B 128.44 m gouge (PSZ-1) (Fig. 1).

7.4. Microstructures formed during experiments on DFDP-1B 128.44 m gouge

In the high-velocity friction experiments conducted on dry 1B 128.44 m gouge, microstructures formed in highly comminuted gouges include clay-clast aggregates (CCAs) and microfoliated gouge layer(s). These microstructures formed at the contact between the sample and wall rock in 2 distinct units that overlie less comminuted gouge (Figs. 8–10). In dry HVFEs on gouge from the Punchbowl Fault, California, USA and Usukidani Fault, Japan, Kitajima et al. (2010) and Boutareaud et al. (2008, 2010) found that CCAs formed when frictional heating in the gouges was sufficient to

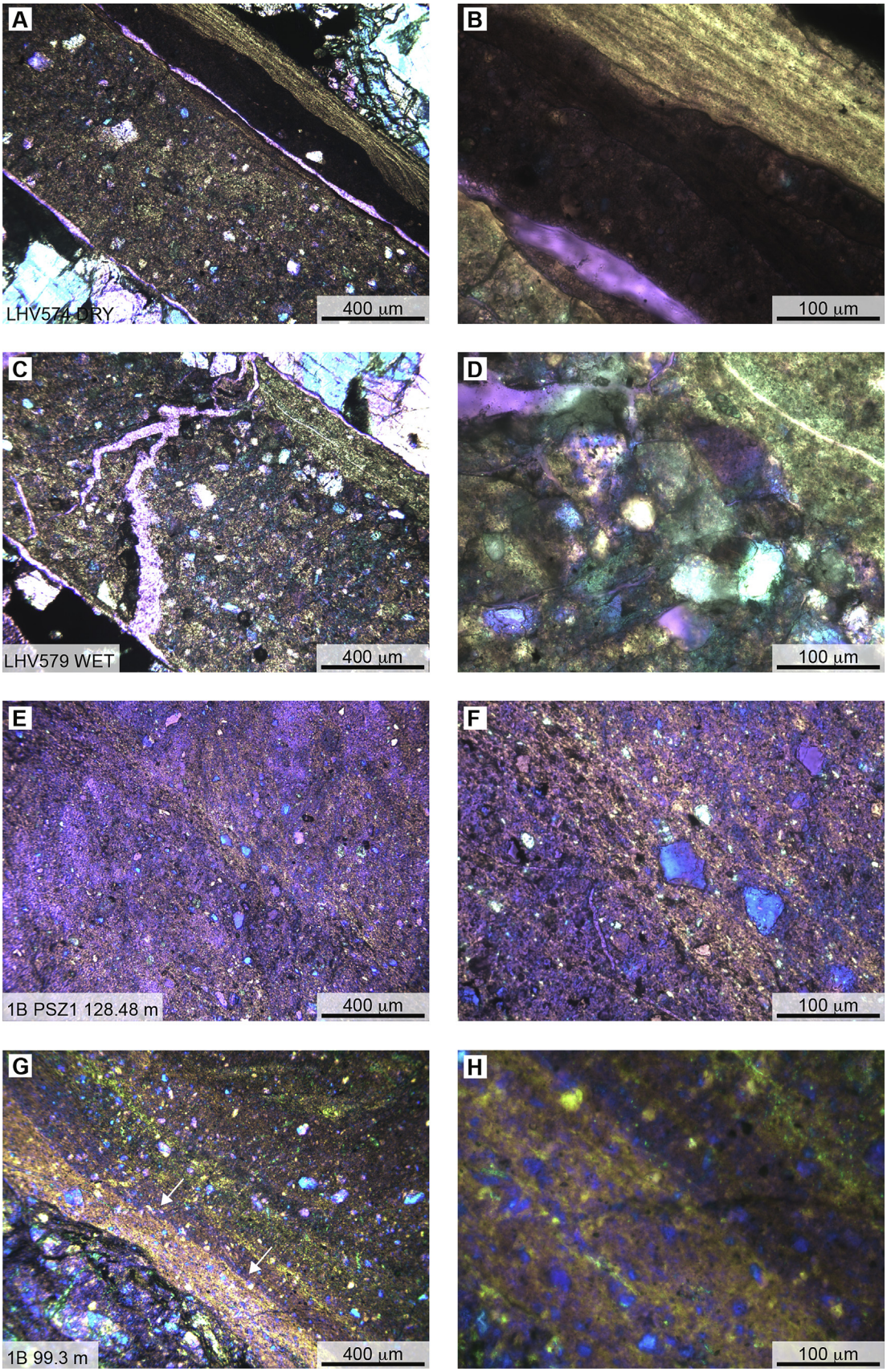

Fig. 12. (a–h) Optical microscope images taken with both polarizers and a full-lambda retarding plate inserted. In these images, microstructures comprising materials with a crystallographic preferred orientation (CPO) appear bright yellow-orange. The (a,b) bright yellow microfoliated gouges formed in the dry high-velocity experiments most closely resemble boundary layers formed between ultramylonite and pseudotachylytes in hanging wall rocks, such as the (g,h) boundary layer (arrow) in the ultramylonite recovered from the DFDP-1B borehole at 99.3 m depth. The (c,d) randomly oriented matrix grains in the reverse-graded layer formed during the wet high-velocity friction experiments resemble matrix grains within natural Alpine Fault PSZ gouges, such as (e,f) PSZ-1 gouge recovered from DFDP-1B at 128.48 m depth. (For interpretation of the references to colour in this figure legend, the reader is referred to the web version of this article.)

cause water vaporization (c. 180 °C at 0.6–1.0 MPa) (Lide, 2008). Boutareaud et al. (2008, 2010) argued that water vaporization creates sufficient pressure to balance or exceed the normal load, allowing the gouge to dilate and fluidize (see also Ferri et al., 2011). These processes facilitate the formation of CCAs through particle rolling.

More recently, quartz clasts with rims of ultrafine grains similar to CCAs were formed during lower displacement (d < 3.72 m), lower velocity (v_{eq} = 0.0005 m/s and 0.08 m/s) dry rotary shear experiments (Han and Hirose, 2012). The observation that CCAs can form at subseismic velocities and low temperatures (<~50 °C) indicates that they are only diagnostic of particle rolling, not frictional sliding at coseismic slip rates (Han and Hirose, 2012; see also Rempe et al., 2014). Warr and Cox (2001) described well-rounded quartz clasts formed within relict friction melts as becoming "snowballed" by smectite during low temperature cataclastic deformation of Alpine Fault gouge at Gaunt Creek. Subsequent authors have cited the "snowballed" clasts as natural examples of CCAs (Boullier et al., 2009; Han and Hirose, 2012), but there is an ongoing debate about whether CCAs form during high-velocity sliding in water-saturated, clay-bearing gouges (Han and Hirose, 2012). Indeed, no CCAs were observed within the 1B 128.44 m gouge deformed wet, or in natural PSZ gouges recovered from DFDP-1B (Figs. 2, 9 and 11).

Nevertheless, gouges containing CCAs and extremely fine-grained microfoliations have been interpreted by many researchers to be the primary slipping zone in dry HVFEs on materials containing phyllosilicates (e.g., Brantut et al., 2008; Boutareaud et al., 2008, 2010; Boullier et al., 2009; Mizoguchi et al., 2009; Kitajima et al., 2010; Ferri et al., 2011; Shimamoto and Togo, 2012; Yao et al., 2013a) (Figs. 8–10). Element maps made on deformed 1B 128.44 m gouge show that the microfoliated gouge layers are enriched in aluminium, iron, and magnesium, and depleted in calcium and silica, relative to coarser-grained gouges (Fig. 10). In addition, these layers display a crystallographic preferred orientation (Fig. 12). These observations suggest that the microfoliated gouge is composed of extremely fine-grained phyllosilicates; compositionally similar material forms the rims of CCAs.

Thermomechanical models indicate that temperatures within the 1B 128.44 m gouge reached ~400 °C during the dry experiments (Fig. 7). If thermal dehydration and/or dehydroxylation did occur at temperatures >150 °C, the multiple microfoliated phyllosilicate layers may have formed when released structural fluids diffused and/or volatilized, causing local strain-hardening and the transfer of slip to weaker materials (cf. Fig. 9a,c and 12b) (see also Hadizedah et al., 2015). Overall, there was no observable difference in the microstructures formed during the dry HVFEs with different velocity histories (Figs. 8–10). Thus, CCA-bearing and microfoliated gouges are likely to be preserved despite small amounts of afterslip, which in this study amounted to ~5–10% of coseismic slip, on the lower end of what is typically expected (Avouac, 2015).

Microstructures formed during the dry HVFEs reflect the preponderance of cataclastic flow processes in the absence of an ambient pore fluid. In cataclastic flow, shearing between grains is accommodated by rolling and sliding of grains along original grain boundaries and along numerous new surfaces created by fracturing and abrasion (controlled particulate flow of Borradaile, 1981). In fluidized gouge, however, grains move past each other without breaking (independent particulate flow of Borradaile, 1981). Gouge fluidization can occur if dilation limits grain-grain interactions and/or if phyllosilicate minerals provide an interconnected matrix capable of accommodating shear along preexisting weak lamellae (Borradaile, 1981; Monzawa and Otsuki, 2003; Ujiie and Tsutsumi, 2010; Bullock et al., 2015). The lack of comminution in the 1B 128.44 m gouge microstructures formed during wet experiments, along with the presence of aligned phyllosilicate lamellae along the upper rotating wall rock, suggests that these gouges underwent fluidization (Figs. 9b,d,11 and 12c,d).

The reverse-graded gouge formed against the lower wall rock provides additional evidence for fluidization (e.g., Figs. 9b,d and 11). Granular materials subjected to particulate flow commonly undergo grain rearrangements wherein small grains migrate into voids beneath larger ones and are forced to remain there by the granular pressure exerted by the overlying larger grains. This type of rearrangement, sometimes termed the "Brazil nut effect," results in the movement of larger grains to the top of shearing and/or vibrating granular aggregates (Williams, 1976; Harwood, 1977; see also Ujiie and Tsutsumi, 2010; Ujiie et al., 2011). Pore fluids enhance size segregation because fluids drag small grains into the void spaces beneath larger ones (Clement et al., 2010).

A comparison between microstructures formed during wet HVFEs on the 1B 128.44 m gouge reveals that 1 m of afterslip caused minor microstructural changes only in the reverse-graded layer (Figs. 8f and 9f). Axial displacement data recorded during low-velocity sliding indicates that the wet gouge compacted continuously during displacement (Fig. 5d). As the pore space requisite for fluidization and size segregation decreased, the large clasts that segregated during fluidized flow were redistributed within the phyllosilicate-rich matrix (Fig. 11e and f). The mixing may have occurred due to shear along phyllosilicate lamellae within the lower layer, which developed a crystallographic preferred orientation oblique to the wall rock (see also Fig. 10 in French et al., 2015).

7.5. Comparison between natural and experimentally produced microstructures

In order to extrapolate experimental results to the Alpine Fault, it is necessary to compare the microstructures formed in the laboratory with those that occur in natural gouge samples (e.g., Rowe and Griffith, 2015). Direct comparison is complicated by the different stress, strain, and temperature-pressure paths followed the natural and experimentally deformed gouges (e.g., Figs. 1 and 2). If the dextral oblique Alpine Fault undergoes serial partitioning into thrust and strike-slip segments at 0.5–2 km depth, the Gaunt Creek thrust segment formed at a maximum depth of 2 km (Barth et al., 2012). The low-temperature alteration mineral smectite present in the PSZ gouges studied could occur along the Alpine Fault at depths up to ~2 km given a geothermal gradient of ~45–65 °C/km (Pytte and Reynolds, 1989; Toy et al., 2010; Sutherland et al., 2012; Boulton et al., 2012).

In drill core, the DFDP-1B PSZ-1 gouge is at least 0.02 m-thick, and the DFDP-1B PSZ-2 gouge is 0.01 m-thick (Fig. 1). Together, the DFDP-1B PSZ gouges have accommodated a total displacement of approximately 5400 m during exhumation from 2 km depth on an oblique thrust fault oriented 059/42 °SE with slickenline striations, which indicate transport direction, plunging 24/086 (Boulton et al., 2017). Assuming strain is distributed between gouge layers, the maximum shear strain experienced by each gouge is ~2 × 10^5 (shear strain, γ, = total displacement/total gouge thickness); this value is an order of magnitude larger than the shear strains accommodated by the experimental gouges (γ~2 × 10^4). In addition, the central Alpine Fault has an average uplift rate of 6–9 mm/yr, and slip is accommodated coseismically by earthquakes with a recurrence interval of 329 ± 68 years (Little et al., 2005; Norris and Cooper, 2007; Berryman et al., 2012). Thus, during 2 km of uplift on the Gaunt Creek thrust segment, the PSZ gouges would have experienced approximately 600–1000 earthquakes. Each earthquake would have triggered fluctuations in fluid pressure, temperature, and pore-fluid chemistry, as indicated by fault gouge

injection veins, authigenic clay mineralization, and strongly pitted clasts of potassium feldspar and calcite (Boulton et al., 2012; Townend et al., 2013; Toy and Mitchell, 2014; Toy et al., 2015a; Schleicher et al., 2015) (Figs. 2b, 10e,f and 11c,d). These complex time-dependent processes are not fully simulated in the laboratory.

Despite these differences, microstructures formed in the wet high-velocity experiments broadly resemble those that occur in the natural gouges, particularly in that matrix grains commonly lack a crystallographic or shape-preferred orientation (Fig. 12). This lack of fabric is interpreted to have resulted from independent particulate flow during shear. Locally, driven by competency contrasts between either rigid clasts or a gouge-wall rock boundary, a transition to laminar flow along weak phyllosilicate lamellae is observed in the experimentally deformed and natural gouges (Figs. 2c,d and 12e-h) (e.g., Goodwin and Tikoff, 2002). Within the natural gouges, these layers are everywhere discontinuous. Our observations are consistent with X-ray goniometer measurements of weak phyllosilicate fabric intensity in both DFDP-1B PSZ gouges (Schleicher et al., 2015). Smectitic fault gouges may have weak fabrics because the irregularly formed smectite microcrystals grow after fault slip ceases (Haines et al., 2009; Schleicher et al., 2015). An alternative explanation for weak fabrics is that the phyllosilicate minerals deformed in a fluidized medium within which the grains were able to move with a mean free path.

Natural PSZ gouges collected from DFDP-1 drill core and nearby outcrops do not contain microstructures similar to the CCA-bearing or microfoliated gouges formed in the dry high-velocity experiments (Boulton et al., 2012, 2014; Toy et al., 2015a; see also Barth et al., 2013). However, microstructures in the Alpine Fault hanging wall associated with pseudotachylytes are comparable to the microfoliated gouges formed during the dry experiments. Alpine Fault pseudotachylytes formed in quartzofeldspathic ultramylonites recovered in DFDP-1B are commonly associated with bounding layers of foliated phyllosilicate minerals and/or ultrafine-grained quartz that formed because of extreme comminution and/or crystallization from melt (Warr and van der Pluijm, 2005; Toy et al., 2011, 2015a) (Fig. 12g and h). While the chemistry and internal structure of these foliated fault rocks varies, the layers do have a CPO similar to that observed in the dry experiments (see also Toy et al., 2015b). The close association of these microstructures with pseudotachylyte and their presence in hanging wall ultramylonites indicates that they formed on subsidiary slip surfaces at seismogenic depths where frictional sliding in anhydrous conditions stimulated comminution and frictional melting (Warr and Cox, 2001; Sibson and Toy, 2006; Toy et al., 2011). Since similar microstructures are not found within the exhumed Alpine Fault PSZ gouges, it is inferred that the PSZ gouges are not likely to exhibit the high peak friction values recorded in the dry experiments.

7.6. Implications for earthquake rupture nucleation and propagation

The high-velocity friction experiments conducted provide evidence that velocity-strengthening PSZ gouges can dynamically weaken at coseismic slip rates of 1 m/s. This dramatic weakening reveals that, as long as rupture energy is sufficient to overcome the low-slip-rate-barrier, Alpine Fault PSZ gouges do not hinder rupture propagation. Furthermore, experimentally determined values of specific fracture energy indicate that it is often energetically favorable for earthquake ruptures to propagate through the wet smectite-bearing PSZ gouges. Whether the propagating rupture tip can provide the acceleration needed to activate dynamic weakening mechanisms in the PSZ gouges depends on its velocity and inertia before entering the velocity-strengthening material. This is governed by the size of the seismic moment up to that point on the fault, which is given by the stress drop and area of velocity-weakening material that nucleated the rupture (and/or failed dynamically) (e.g., Noda et al., 2009; Kozdon and Dunham, 2013). Other key variables include the magnitude and velocity-dependence of (a-b) in the velocity-strengthening gouges (e.g., Marone, 1998; Perfettini and Ampuero, 2008), the areal distribution of velocity-strengthening and velocity-weakening materials (e.g., Hillers et al., 2006; Noda and Lapusta, 2013), and the dampening effects of dilatancy strengthening (e.g., Segall and Rice, 1995; Samuelson et al., 2009; Segall et al., 2010). Indeed, frictional failure of the Alpine Fault requires the presence of velocity-weakening material in a nucleation patch as well as sufficient resolved shear stress to overcome its frictional strength. Once nucleated, the complex interplay between resolved shear stress, peak strength, dynamic strength loss, slip-weakening distance, and dynamic strength recovery in lithologically heterogeneous materials governs rupture propagation rate, the mode of rupture propagation, and the frequency and amplitude of radiated energy that dictates ground motion (Beeler, 2006; Rice and Cocco, 2007; Ben-Zion, 2008; Noda et al., 2009; Noda and Lapusta, 2013).

8. Conclusions

1. In room-dry high-velocity friction experiments, the peak coefficients of friction (μ_p) of phyllosilicate-poor cataclasites and phyllosilicate-rich gouges and cataclasites were consistently high (mean $\mu_p = 0.67 \pm 0.07$; $n = 11$).
2. In wet high-velocity friction experiments, the peak coefficients of friction of the phyllosilicate-poor cataclasites (mean $\mu_p = 0.63 \pm 0.06$; $n = 2$) were higher than those of the phyllosilicate-rich gouges and cataclasites (mean $\mu_p = 0.27 \pm 0.21$; $n = 8$).
3. All Alpine Fault rocks tested in room-dry and wet conditions exhibited very low steady-state coefficients of friction (mean $\mu_{ss} = 0.14 \pm 0.06$; $n = 21$).
4. The six experiments conducted on wet smectite-bearing PSZ fault gouges yielded the lowest peak friction coefficients ($\mu_p = 0.10–0.20$) and lowest steady-state friction coefficients ($\mu_{ss} = 0.04–0.10$).
5. Measured values of peak friction coefficients and specific fracture energy indicate that, given sufficient acceleration, rupture propagation through smectite-bearing PSZ fault gouges is often energetically favorable compared with other fault gouges and cataclasites tested.
6. Microstructural observations and interpretations indicate that natural PSZ gouges recovered from DFDP-1 drill core most closely resemble gouges produced during the wet high-velocity friction experiments.
7. The shallowest portion of the Alpine Fault (<~2 km depth, depending on geothermal gradient), wherein smectite is thermodynamically stable, is expected to exhibit low values of peak friction and steady-state friction during a seismic event.

Acknowledgements

This research was made possible by the support of the Institute of Geology, China Earthquake Administration, Beijing, China and grant LED2014A06 awarded to S. Ma. In addition, the following people, companies, and institutions made the Deep Fault Drilling Project (DFDP-1) successful: Horizon Drilling, Alex Pyne, the New Zealand Department of Conservation, the Marsden Fund, GNS Science, Victoria University of Wellington and the Universities of Otago, Auckland, Canterbury, Liverpool, and Bremen. The first author would like to thank Brent Pooley, Paul Hands, and Mark Raven for technical assistance with thin-section making and X-ray

diffraction. Michael J. Allen kindly provided images 12g and 12h. E. Mariani, C. Pennington, and the University of Liverpool Earth Science EBSD-SEM laboratories are thanked for the provision and maintenance of excellent microscopy facilities. CB and DRF acknowledge NERC support from grant NE/J024449/1. This manuscript benefited greatly from suggestions made by H. Kitajima and two anonymous reviewers. Experimental data and model results are freely available from the corresponding author.

Appendix A. Supplementary data

Supplementary data related to this article can be found at http://dx.doi.org/10.1016/j.jsg.2017.02.003.

References

Andrews, D., 2002. A fault constitutive relation accounting for thermal pressurization of pore fluid. J. Geophys. Res. 107 (B12), 2363. http://dx.doi.org/10.1029/2002JB001942.

Avouac, J.-P., 2015. From geodetic imaging of seismic and aseismic fault slip to dynamic modeling of the seismic cycle. Annu. Rev. Earth Planet. Sci. 43, 233–271. http://dx.doi.org/10.1146/annurev-earth-060614-105302.

Barth, N.C., Toy, V.G., Langridge, R.M., Norris, R.J., 2012. Scale dependence of oblique plate-boundary partitioning: new insights from LiDAR, central Alpine fault, New Zealand. Lithosphere. http://dx.doi.org/10.1130/L201.1. L201.

Barth, N.C., Boulton, C., Carpenter, B.M., Batt, G., Toy, V.G., 2013. Slip localization on the southern Alpine Fault, New Zealand. Tectonics 32, 1–21.

Beeler, N.M., 2006. Inferring earthquake source properties from laboratory observations and the scope of lab contributions to source physics. In: Abercrombie, R., McGarr, A., Kanamori, H., Di Toro, G., Earthquakes (Eds.), Radiated Energy and the Physics of Faulting, Geophysical Monograph, vol. 170. American Geophysical Union, pp. 99–119.

Beeler, N.M., Tullis, T.E., Goldsby, D.L., 2008. Constitutive relationships and physical basis of fault strength due to flash heating. J. Geophys. Res. 113, B01401. http://dx.doi.org/10.1029/2007JB004988.

Ben-Zion, Y., 2008. Collective behavior of earthquakes and faults: continuum-discrete transitions, progressive evolutionary changes, and different dynamic regimes. Rev. Geophy 46, RG4006. http://dx.doi.org/10.1029/2008RG000260.

Berryman, K.B., Cochran, U.A., Clark, K.J., Biasi, G.P., Langridge, R.M., Villamor, P., 2012. Major earthquakes occur regularly on an isolated plate boundary fault. Science 29 (336), 1690–1693. http://dx.doi.org/10.1126/science.1218959.

Bizarri, A., Cocco, M., 2006a. A thermal pressurization model for the spontaneous dynamic rupture propagation on a three-dimensional fault: 1.Methodological approach. J. Geophys. Res. 111, B05303. http://dx.doi.org/10.1029/2005JB003862.

Bizarri, A., Cocco, M., 2000b. A thermal pressurization model for the spontaneous dynamic rupture propagation on a three-dimensional fault: 2. Traction evolution and dynamic parameters. J. Geophys. Res. 111, B05304. http://dx.doi.org/10.1029/2005JB003864.

Borradaile, G.J., 1981. Particulate flow of rock and the formation of cleavage. Tectonophysics 72, 305–321.

Boullier, A.-M., Yeh, E.-C., Boutareaud, S., Song, S.-R., Tsai, C.-H., 2009. Microscale anatomy of the 1999 Chi-Chi earthquake fault zone. Geochem. Geophys. Geosys 10 (3), Q03016. http://dx.doi.org/10.1029/2008GC002252.

Boulton, C., Carpenter, B.M., Toy, V.G., Marone, C., 2012. Physical properties of surface outcrop cataclastic fault rocks, Alpine Fault, New Zealand. Geochem. Geophys. Geosys. 13, Q01018. http://dx.doi.org/10.1029/2011GC003872.

Boulton, C., Moore, D.E., Lockner, D.A., Toy, V.G., Townend, J., Sutherland, R., 2014. Frictional strength and stability of exhumed fault gouges in DFDP-1 cores, Alpine Fault, New Zealand. Geophys. Res. Lett. 41 http://dx.doi.org/10.1002/2013GL058236.

Boulton, C., Menzies, C.D., Toy, V.G., Townend, J., Sutherland, R., 2017. Geochemical and microstructural evidence for interseismic changes in fault zone permeability and strength, Alpine Fault, New Zealand. Geochem. Geophys. Geosyst. 18 http://dx.doi.org/10.1002/2016GC006588.

Boutareaud, S., Calugaru, D.-G., Han, R., Fabbri, O., Mizoguchi, K., Tsutsumi, A., Shimamoto, T., 2008. Clay-clast aggregates: a new textural evidence for seismic fault sliding? Geophys. Res. Lett. 35, L05302. http://dx.doi.org/10.1029/2007GL032554.

Boutareaud, S., Boullier, A.-M., Andreani, M., Calugaru, D.-G., Beck, P., Song, S.-R., Shimamoto, T., 2010. Clay-clast aggregates in gouges: a new textural evidence for seismic faulting. J. Geophys. Res. 115, B02408. http://dx.doi.org/10.1029/2008JB006254.

Brantut, N., Schubnel, A., Rouzaud, J.-N., Brunet, F., Shimamoto, T., 2008. High velocity frictional properties of a clay-bearing fault gouge and implications for earthquake mechanics. J. Geophys. Res. 113, B10401. http://dx.doi.org/10.1029/2007JB005551.

Brantut, N., Han, R., Shimamoto, T., Findling, N., Schubnel, A., 2011. Fast slip with inhibited temperature rise due to mineral dehydration: evidence from experiments on gypsum. Geology 39, 59–62. http://dx.doi.org/10.1130/G31424.1.

Brodsky, E.E., Kanamori, H., 2001. Elastohydrodynamic lubrication of faults. J. Geophys. Res. 106 (B8), 16357–16374. http://dx.doi.org/10.1029/2001JB000430.

Bullock, R.J., De Paola, N., Holdsworth, R.E., 2015. An experimental investigation in the role of phyllosilicate content on earthquake propagation during seismic slip in carbonate faults. J. Geophys. Res. Solid Earth 120, 3187–3207. http://dx.doi.org/10.1002/2015JB011914.

Byerlee, J., 1978. Friction of rocks. Pure App. Geophys. 116, 615–626.

Carpenter, B.M., Kitajima, H., Saffer, D.M., 2014. Permeability and elastic properties of the active Alpine Fault, New Zealand: measurements on shallow drill core. Earth Planet. Sci. Lett. 390, 45–51. http://dx.doi.org/10.1016/j.epsl.2013.12.023.

Chang, J., Lockner, D.A., Reches, Z., 2012. Rapid acceleration leads to rapid weakening in earthquake-like laboratory experiments. Science 338 (6103), 101–105.

Chen, J., Yang, X., Duan, Q., Shimamoto, T., Spiers, C.J., 2013. Importance of thermochemical pressurization in the dynamic weakening of the Longmenshan Fault during the 2008 Wenchuan earthquake: inferences from experiments and modeling. J. Geophys. Res. Solid Earth 118, 1–25. http://dx.doi.org/10.1002/jgrb.50260.

Chen, J., Niemeijer, A.R., Yao, L., Ma, S., 2017. Water vaporization promotes coseismic fluid pressurization and buffers temperature rise. Geophys. Res. Lett. http://dx.doi.org/10.1002/2016GL071932.

Clement, C.P., Pancheco-Martinez, H.A., Swift, M.R., King, P.J., 2010. The water-enhanced Brazil nut effect. EPL 91, 54001. http://dx.doi.org/10.1029/0295-5075/91/54011.

Cocco, M., Tinti, E., 2008. Scale dependence in the dynamics of earthquake propagation: evidence from seismological and geological observations. Earth Planet. Sci. Lett. 273, 123–131. http://dx.doi.org/10.1016/j.epsl.2008.06.025.

De Paola, N., Hirose, T., Mitchell, T., Di Toro, G., Viti, C., Shimamoto, T., 2011. Fault lubrication and earthquake propagation in thermally unstable rocks. Geology 39 (1), 35–38. http://dx.doi.org/10.1130/G31398.1.

Di Toro, G., Goldsby, D.L., Tullis, T.E., 2004. Friction falls towards zero in quartz rock as slip velocity approaches seismic rates. Nature 427, 436–439.

Di Toro, G., Han, R., Hirose, T., De Paola, N., Nielsen, S., Mizoguchi, K., Ferri, F., Cocco, M., Shimamoto, T., 2011. Fault lubrication during earthquakes. Nature 471, 494–499. http://dx.doi.org/10.1038/nature09838.

Faulkner, D.R., Mitchell, T.M., Behnsen, J., Hirose, T., Shimamoto, T., 2011. Stuck in the mud? Earthquake nucleation and propagation through accretionary forearcs. Geophys. Res. Lett. 38 http://dx.doi.org/10.1039/2011GL048552.

Ferri, F., Di Toro, G., Hirose, T., Han, R., Noda, H., 2011. Low- to high velocity frictional properties of the clay-rich gouges from the slipping zone of the 1963 Vaiont slide, northern Italy. J. Geophys. Res. 116, B09208. http://dx.doi.org/10.1029/2011JB008338.

French, M.E., Kitajima, H., Chester, J.S., Chester, F.M., Hirose, T., 2014. Displacement and dynamic weakening processes in smectite-rich gouge from the central deforming zone of the san andreas fault. J. Geophys. Res. Solid Earth 119. http://dx.doi.org/10.1002/2013JB010757.

French, M.E., Chester, F.M., Chester, J.S., 2015. Micromechanisms of creep in clay-rich gouge from the Central Deforming Zone of the San Andreas Fault. J. Geophys. Res. Solid Earth 120. http://dx.doi.org/10.1002/2014JB011496.

Fulton, P.M., Rathbun, A.P., 2011. Experimental constraints on energy partitioning during stick-slip and stable sliding within analog fault gouge. Earth Planet. Sci. Lett. 308, 185–192. http://dx.doi.org/10.1016/j.epsl.2011.05.051.

Garagash, D.I., 2012. Seismic and aseismic slip pulses driven by thermal pressurization of pore fluid. J. Geophys. Res. 117, B04314. http://dx.doi.org/10.1029/2011JB008889, 37pp.

Garagash, D.I., Rudnicki, J., 2003. Shear heating of a fluid-saturated slip-weakening dilatant fault zone 1. Limiting regimes. J. Geophys. Res. 10 http://dx.doi.org/10.1029/2001JB001653.

Garagash, D.I., Germanovitch, L.N., 2012. Nucleation and arrest of dynamic slip on a pressurized fault. J. Geophys. Res. 117, B10310. http://dx.doi.org/10.1029/2012JB009209.

Goldsby, D.L., Tullis, T.E., 2002. Low frictional strength of quartz rocks at subseismic slip rates. Geophys. Res. Lett. 29 (17), 1844. http://dx.doi.org/10.1029/2002GL015240.

Goldsby, D.L., Tullis, T.E., 2011. Flash heating leads to low frictional strength of crustal rocks at earthquake slip rates. Science 334, 216–218.

Goodwin, L.B., Tikoff, B., 2002. Competency contrast, kinematics, and the development of foliations and lineations in the crust. J. Struct. Geol. 24, 1065–1085.

Hadizedah, J., Tullis, T.E., White, J.C., Konkachbaev, A.I., 2015. Shear localization, velocity weakening behavior, and development of cataclastic foliation in experimental granite gouge. J. Struct. Geol. 71, 86–99. http://dx.doi.org/10.1016/j.jsg.2014.10.013.

Haines, S.H., van der Pluijm, B.A., Ikari, M.J., Saffer, D.M., Marone, C., 2009. Clay fabric intensity in natural and artificial fault gouges: implications for brittle fault zone process and sedimentary basin clay fabric evolution. J. Geophys. Res. 114, B05406. http://dx.doi.org/10.1029/2008JB005866.

Han, R., Hirose, T., 2012. Clay-clast aggregates in fault gouge: an unequivocal indicator of seismic faulting at shallow depths? J. Struct. Geol. 43, 92–99. http://dx.doi.org/10.1016/j.jsg.2012.07.008.

Han, R., Hirose, T., Shimamoto, T., 2010. Strong velocity weakening and powder lubrication of simulated carbonate faults at seismic slip rates. J. Geophys. Res. 115, B03412. http://dx.doi.org/10.1029/2008JB006136.

Han, R., Hirose, T., Shimamoto, T., Lee, Y., Ando, J., 2011. Granular nanoparticles lubricate faults during seismic slip. Geology 39 (6), 599–602.

Harwood, C.F., 1977. Powder segregation due to vibration. Powder Technol. 16,

51–57. http://dx.doi.org/10.1016/0032-5910(77)85020-1.
Hillers, G., Ben-Zion, Y., Mai, P., 2006. Seismicity on a fault controlled by rate and state-dependent friction with spatial variations of the critical slip distance. J. Geophys. Res. 111, B01403. http://dx.doi.org/10.1029/2005JB003859.
Hirono, T., Tanikawa, W., Honda, G., Kameda, J., Fukuda, J., Ishikawa, T., 2013. Importance of mechanochemical effects on fault slip behavior during earthquakes. Geophys. Res. Lett. 40, 2988–2992. http://dx.doi.org/10.1002/grl.50609.
Hirose, T., Shimamoto, T., 2005. Growth of molten zone as a mechanism of slip weakening of simulated faults in gabbro during frictional melting. J. Geophys. Res. Solid Earth 110, B05202. http://dx.doi.org/10.1029/2004JB003207.
Ikari, M.J., Saffer, D.M., Marone, C., 2009. Frictional and hydrologic properties of clay-rich fault gouge. J. Geophys. Res. 114, B05409. http://dx.doi.org/10.1029/2008JB006089.
Ikari, M.J., Carpenter, B.M., Kopf, A.J., Marone, C., 2014. Frictional strength, rate-dependence, and healing in DFDP-1 borehole samples from the Alpine Fault, New Zealand. Tectonophysics 630, 1–8.
Kitajima, H., Chester, J.S., Chester, F.M., Shimamoto, T., 2010. High-speed friction of disaggregated ultracataclasite in rotary shear: characterization of frictional heating, mechanical behavior, and microstructure evolution. J. Geophys. Res. 115 http://dx.doi.org/10.1029/2009JB007038.
Koster van Groos, A.F., Guggenheim, S., 1984. The effect of pressure on the dehydration reaction of interlayer water in Na-montmorillonite (SWy-1). Am. Mineral. 69 (9–10), 872–879.
Kozdon, J., Dunham, E., 2013. Rupture to the trench: dynamic rupture simulations of the 11 March 2011 Tohoku Earthquake. Bull. Seis. Soc. Am. 103 (2B), 1275–1289.
Lachenbruch, A.H., 1980. Frictional heating, fluid pressure, and the resistance to fault motion. J. Geophys. Res. 85 (B11), 6097–6112.
Lide, D., 2008. CRC Handbook of Chemistry and Physics, 89th Edition. CRC Press. ISBN 142006679X.
Little, T.A., Cox, S., Vry, J.K., Batt, G., 2005. Variations in exhumation level and uplift rate along the oblique-slip Alpine fault, central Southern Alps, New Zealand. Geol. Soc. Am. Bull. 117 (5/6), 707–723.
Ma, S., Shimamoto, T., Yao, L., Togo, T., Kitajima, H., 2014. A rotary-shear low to high-velocity friction apparatus in Beijing to study rock friction at plate to seismic slip rates. Earthq. Sci. 27 (5), 469–497. http://dx.doi.org/10.1007/s11589-014-0097-5.
Marone, C., 1998. Laboratory-derived friction laws and their application to seismic faulting. Ann. Rev. Earth Planet. Sci. 26, 643–696.
Mizoguchi, K., 2005. High-velocity Frictional Behavior of Nojima Fault Gouge and its Implications for Seismogenic Fault Motion. Ph.D. thesis. Kyoto University, Kyoto, Japan.
Mizoguchi, K., Hirose, T., Shimamoto, T., Fukuyama, E., 2007. Reconstruction of seismic faulting by high-velocity friction experiments: an example of the 1995 Kobe earthquake. Geophys. Res. Lett. 34, L01308. http://dx.doi.org/10.1029/2006GL027931.
Mizoguchi, K., Hirose, T., Shimamoto, T., Fukuyama, E., 2009. High-velocity frictional behavior and microstructure evolution of fault gouge obtained from Nojima fault, southwest Japan. Tectonophysics 471, 285–296. http://dx.doi.org/10.1016/j.tecto.2009.02.033.
Monzawa, N., Otsuki, K., 2003. Comminution and fluidization of granular fault materials: implications for fault slip behavior. Tectonophysics 367 (1–2), 127–143.
Niemeijer, A., Di Toro, G., Griffith, W.A., Bistachhi, A., Smith, S.A.F., Nielsen, S., 2012. Inferring earthquake physics and chemistry using an integrated field and laboratory approach. J. Struct. Geol. http://dx.doi.org/10.1016/j.jsg.2012.02.018.
Niemeijer, A.R., Boulton, C., Toy, V.G., Townend, J., Sutherland, R., 2016. Large-displacement, hydrothermal frictional properties of DFDP-1 fault rocks, Alpine Fault, New Zealand: implications for deep rupture propagation. J. Geophys. Res. 121 http://dx.doi.org/10.1002/2015JB012593.
Nielsen, S., Di Toro, G., Hirose, T., Shimamoto, T., 2008. Frictional melt and seismic slip. J. Geophys. Res. 113, B01308. http://dx.doi.org/10.1029/2007JB005122.
Nielsen, S.B., Spagnuolo, E., Violay, M., Di Toro, G., 2013. Friction at seismic slip rates: Testing thermal weakening models experimentally. In: Abstract MR42A-07 presented at 2013 Fall Meeting, AGU, San Francisco, California, 9–13 December.
Noda, H., Shimamoto, T., 2009. Constitutive properties of clayey fault gouge from the Hanaore fault zone, southwest Japan. J. Geophys. Res. 114, B04409. http://dx.doi.org/10.1029/2008JB005683.
Noda, H., Lapusta, N., 2013. Stable creeping fault segments can become destructive as a result of dynamic weakening. Nature. http://dx.doi.org/10.1038/nature11703.
Noda, H., Dunham, E.M., Rice, J.R., 2009. Earthquake ruptures with thermal weakening and the operation of major faults at low overall stress levels. J. Geophys. Res. 114, B07302. http://dx.doi.org/10.1029/2008JB006143.
Norris, R.J., Cooper, A.F., 2007. The Alpine Fault, New Zealand: surface geology and field relationships. In: Okaya, D., Stern, T., Davey, F. (Eds.), A Continental Plate Boundary: Tectonics at South Island, New Zealand, Geophys. Monogr. Ser, vol. 175. AGU, Washington, D.C, pp. 159–178.
Oohashi, K., et al., 2015. Graphite as a lubricating agent in fault zones: an insight from low- to high-velocity friction experiments on a mixed graphite-quartz gouge. J. Geophys. Res. Solid Earth 118, 2067–2084. http://dx.doi.org/10.1002/jgrb.50175.
Passelègue, F.X., Goldsby, D.L., Fabbri, O., 2014. The influence of ambient fault temperature on flash-heating phenomena. Geophys. Res. Lett. 41, 828–835. http://dx.doi.org/10.1002/2013GL058374.
Perfettini, H., Ampuero, J.-P., 2008. Dynamics of a velocity strengthening region: implications for slow earthquakes and postseismic slip. J. Geophys. Res. 113 (B9), B09317. http://dx.doi.org/10.1029/2007JB005553.
Platt, J.D., Viesca, R.C., Garagash, D.I., 2015. Steadily propagating slip pulses driven by thermal decomposition. J. Geophys. Res. Solid Earth 120, 6558–6591. http://dx.doi.org/10.1002/2015JB012200.
Platt, J.D., Proctor, B.P., Mitchell, T.M., Hirth, G., Goldsby, D.L., Di Toro, G., Beeler, N.M., Tullis, T.E., 2014. The role of gouge and temperature in flash heating and its hysteresis. In: Abstract S11C-4360 presented at 2014 Fall Meeting, AGU, San Francisco, California, 15–19 December.
Proctor, B.P., Mitchell, T.M., Hirth, G., Goldsby, D., Zorzi, F., Platt, J.D., Di Toro, G., 2014. Dynamic weakening of serpentinite gouges and bare surfaces at seismic slip rates. J. Geophys. Res. Solid Earth 119. http://dx.doi.org/10.1002/2014JB011057.
Pytte, A.M., Reynolds, R.C., 1989. The Thermal Transformation of Smectite to Illite. Springer, New York.
Reches, Z., Lockner, D.A., 2010. Fault weakening and earthquake instability by powder lubrication. Nature 467, 452–456. http://dx.doi.org/10.1038/nature09348.
Remitti, F., Smith, S.A.F., Mittempergher, S., Gualtieri, A.F., Di Toro, G., 2015. Frictional properties of fault zone gouges from the J-Fast drilling project (Mw 9.0 Tohoku-Oki earthquake). Geophys. Res. Lett. 42, 2691–2699. http://dx.doi.org/10.1002/2015GL063507.
Rempe, M., Smith, S.A.F., Ferri, F., Mitchell, T.M., Di Toro, G., 2014. Clast-cortex aggregates in experimental and natural calcite-bearing fault zones. J. Struct. Geol. 68, 142–157.
Rice, J.R., 2006. Heating and weakening of faults during earthquake slip. J. Geophys. Res. 111 (B5), B05311. http://dx.doi.org/10.1029/2005JB004006.
Rice, J.R., Cocco, M., 2007. Seismic fault rheology and earthquake dynamics. In: Handy, M.R., Hirth, G., Hovius, N. (Eds.), Tectonic Faults: Agents of Change on a Dynamic Earth. The MIT Press, Cambridge, USA.
Rowe, C.D., Griffith, W.A., 2015. Do faults preserve a record of seismic slip: a second opinion. J. Struct. Geol. 78, 1–26.
Samuelson, J., Elsworth, D., Marone, C., 2009. Shear-induced dilatancy of fluid-saturated faults: experiment and theory. J. Geophys. Res. 114, B12404. http://dx.doi.org/10.1029/2008JB006273.
Sawai, M., Shimamoto, T., Togo, T., 2012. Reduction in BET surface area of Nojima fault gouge with seismic slip and its implication for the fracture energy of earthquakes. J. Struct. Geol. 38, 117–138.
Schleicher, A.M., Sutherland, R., Townend, J., Toy, V.G., van der Pluijm, B.A., 2015. Clay mineral formation and fabric development in the DFDP-1B borehole, central Alpine Fault, New Zealand. N. Z. J. Geol. Geophys. 58 (1), 13–21.
Schmitt, V.S., Segall, P., Matsuzawa, T., 2011. Shear heating-induced thermal pressurization during earthquake nucleation. J. Geophys. Res. 116, B06308. http://dx.doi.org/10.1029/2010JB008035.
Scholz, C.H., 1998. Earthquakes and friction laws. Nature 391, 37–42.
Scholz, C.H., 2002. The Mechanics of Earthquakes and Faulting, second ed. Cambridge Press, p. 471.
Segall, P., Rice, J.R., 1995. Dilatancy, compaction, and slip instability of a fluid-infiltrated fault. J. Geophys. Res. 100, 22155–22171. http://dx.doi.org/10.1029/95JB02403.
Segall, P., Rubin, A., Bradley, A., Rice, J.R., 2010. Dilatant strengthening as a mechanism for slow slip events. J. Geophys. Res. 115, B12305. http://dx.doi.org/10.1029/2010JB007449.
Shimamoto, T., Logan, J., 1981. Effects of simulated clay gouges on the sliding behavior of Tennessee sandstone. Tectonophysics 75, 243–255.
Shimamoto, T., Tsutsumi, A., 1994. A new rotary-shear high-speed frictional testing machine: its basic design and scope of research (in Japanese with English abstract). J. Tecton. Res. Group Jpn. 39, 65–78.
Shimamoto, T., Togo, T., 2012. Earthquakes in the lab. Science 338, 54–55.
Sibson, R.H., 1973. Interactions between temperature and pore-fluid pressure during earthquake faulting and a mechanism for partial or total stress relief. Nature 243, 66–68.
Sibson, R.H., 1977. Fault rocks and fault mechanisms. J. Geol. Soc. Lond. 133, 191–213.
Sibson, R.H., Toy, V.G., 2006. The habitat of fault-generated pseudotachylyte: presence vs. absence of friction melt. In: Abercrombie, R., McGarr, A., Kanamori, H., Di Toro, G., Earthquakes (Eds.), Radiated Energy and the Physics of Faulting, Geophysical Monograph, vol. 170. American Geophysical Union, pp. 153–166.
Sone, H., Shimamoto, T., 2009. Frictional resistance of faults during accelerating and decelerating earthquake slip. Nat. Geosci. 2, 705–708. http://dx.doi.org/10.1038/NGEO637.
Sulem, J., Lazar, P., Vardoulakis, I., 2007. Thermo-poro-mechanical properties of clayey gouge and application to rapid fault shearing. Int. J. Numer. Anal. Met. 31, 523–540.
Sutherland, R., Davey, F., Beavan, J.P., 2000. Plate boundary deformation in South Island, New Zealand, is related to inherited lithospheric structure. Earth Planet. Sci. Lett. 177, 141–151.
Sutherland, R., et al., 2007. Do great earthquakes occur on the Alpine fault in central South Island, New Zealand? In: Okaya, D., et al. (Eds.), A Continental Plate Boundary: Tectonics at South Island, New Zealand, Geophysical Monograph, vol. 175. American Geophysical Union, pp. 235–251.
Sutherland, R., et al., 2012. Drilling reveals fluid control on architecture and rupture of the Alpine Fault, New Zealand. Geology 40, 1143–1146. http://dx.doi.org/10.1130/G33614.1.

Tanikawa, W., Shimamoto, T., 2009. Frictional and transport properties of the Chelungpu fault from shallow borehole data and their correlation with seismic behavior during the 1999 Chi-Chi earthquake. J. Geophys. Res. 114, B01402. http://dx.doi.org/10.1029/2008JB005750.

Tanikawa, W., Mukoyoshi, H., Tadai, O., Hirose, T., Tsutsumi, A., Lin, W., 2012. Velocity dependence of shear-induced permeability associated with frictional behavior in fault zones of the Nankai subduction zone. J. Geophys. Res. 117, B05405. http://dx.doi.org/10.1029/2011JB008956.

Tembe, S., Lockner, D.A., Wong, T.F., 2010. Effect of clay content and mineraology on frictional sliding behavior of simulated gouges: binary and ternary mixtures of quartz, illite, and montmorillonite. J. Geophys. Res. 115, B03416. http://dx.doi.org/10.1029/2009JB006383.

Togo, T., Shimamoto, T., Ma, S., Hirose, T., 2011. High-velocity frictional behavior of Longmenshan fault gouge from Hongkou outcrop and its implications for dynamic weakening of fault during 2008 Wenchuan earthquake. Earthq. Sci. 24, 267–281.

Townend, J., Sutherland, R., Toy, V.G., Eccles, J.D., Boulton, C.J., Cox, S.C., McNamara, D., 2013. Late-interseismic state of a continental plate-bounding fault: petrophysical results from DFDP-1 wireline and core analysis, Alpine fault, New Zealand. Geochem., Geophys., Geosyst. 14 http://dx.doi.org/10.1002/ggge/20236.

Toy, V.G., Mitchell, T.M., 2014. Photograph of the month. J. Struct. Geol. 64 (1), iii. http://dx.doi.org/10.1016/SO191-8141(14)00094-7.

Toy, V.G., Craw, D., Cooper, A.F., Norris, R.J., 2010. Thermal regime in the central Alpine Fault zone, New Zealand: constraints from microstructures, biotite chemistry and fluid inclusion data. Tectonophysics. http://dx.doi.org/10.1016/j.tecto.2009.12.013.

Toy, V.G., Ritchie, S., Sibson, R.H., 2011. Diverse habitats of pseudotachylytes in the Alpine fault zone and relationships to current seismicity. In: Fagereng, Å., Toy, V.G., Rowland, J.V. (Eds.), Geology of the Earthquake Source: a Volume in Honour of Rick Sibson, Geol. Soc. London Special Pub, vol. 359, pp. 115–133.

Toy, V.G., Boulton, C.J., Sutherland, R., Townend, J., Norris, R.J., Little, T.A., Prior, D.J., Mariani, E., Faulkner, D.R., Menzies, C.D., Scott, H., Carpenter, B.M., 2015a. Fault rock lithologies and architecture of the central Alpine fault, New Zealand, revealed by DFDP-1 drilling. Lithosphere. http://dx.doi.org/10.1130/L395.1.

Toy, V.G., Mitchell, T.M., Druiventak, A., Wirth, R., 2015b. Crystallographic preferred orientations may develop in nanocrystalline materials on fault planes due to surface energy interactions. Geochem, Geophys, Geosyst 16. http://dx.doi.org/10.1002/2015GC005857.

Tsutsumi, A., Shimamoto, T., 1997. High-velocity frictional properties of gabbro. Geophy. Res. Lett. 24 (6), 699–702.

Ujiie, K., Tsutsumi, A., 2010. High-velocity frictional properties of clay-rich fault gouge in a megasplay fault zone, Nakai subduction zone. Geophys. Res. Lett. 37, L24310. http://dx.doi.org/10.1029/2010GL046002.

Ujiie, K., Tsutsumi, A., Kameda, J., 2011. Reproduction of thermal pressurization and fluidization of clay-rich fault gouges by high-velocity friction experiments and implications for seismic slip in natural faults. In: Fagereng, Å., Toy, V.G., Rowland, J.V. (Eds.), Geology of the Earthquake Source: a Volume in Honour of Rick Sibson, Geol. Soc. London Special Pub, vol. 359, pp. 267–285.

Ujiie, K., et al., 2013. Low coseismic shear stress on the Tohoku-Oki Megathrust determined from laboratory experiments. Science 342 (6163), 1211–1214. http://dx.doi.org/10.1126/science.1243485.

Violay, M., Di Toro, G., Nielsen, S., Spagnuolo, E., Burg, J.P., 2015. Thermo-mechanical pressurization of experimental faults in cohesive rocks during seismic slip. Earth Planet. Sci. Lett. 429, 1–10.

Warr, L.N., Cox, S., 2001. Clay mineral transformations and weakening mechanisms along the Alpine Fault, New Zealand. In: Holdsworth, R.E., Strachan, R.A., Magloughlin, J.F., Knipe, R.J. (Eds.), The Nature and Tectonic Significance of Fault Zone Weakening, Geol. Soc. London Spec. Pub, vol. 186, pp. 85–101.

Warr, L.N., van der Pluijm, B.A., 2005. Crystal fractionation in the frictional melts of seismic faults (Alpine Fault, New Zealand). Tectonophysics 402, 111–124.

Wellman, H.W., 1953. Data for the study of recent and late pleistocene faulting in the south Island of New Zealand. N. Z. J. Sci. Tech. 34B, 270–288.

Wells, A., Goff, J., 2007. Coastal dunes in Westland, New Zealand, provide a record of paleoseismic activity on the Alpine fault. Geology 35 (8), 731–734.

Wibberley, C.A.J., Shimamoto, T., 2005. Earthquake slip weakening and asperities explained by thermal pressurization. Nature 436, 689–692. http://dx.doi.org/10.1038/nature03901.

Wibberley, C.A.J., Yielding, G., Di Toro, G., 2008. Recent advances in the understanding of fault zone internal structure: a review. In: Wibberley, C.A.J., Kurz, W., Imber, J., Holdsworth, R.E., Collettini, C. (Eds.), The Internal Structure of Fault Zones: Implications for Mechanical and Fluid-flow Properties, Geol. Soc. London Spec. Pub, vol. 299, pp. 5–33.

Williams, J.C., 1976. The segregation of particulate materials. A review. Powder Technol. 15, 245–251. http://dx.doi.org/10.1016/0032-5910(76)80053-8.

Yao, L., Shimamoto, T., Togo, T., Ma, S., 2013a. Structures and high-velocity friction properties of the Pingxi fault zone in the Longmenshan fault system, Sichian, China, activation during the 2008 Wenchuan earthquake. Tectonophysics 599, 135–156. http://dx.doi.org/10.1016/j.tecto.2013.04.011.

Yao, L., Shimamoto, T., Ma, S., Han, R., Mizoguchi, K., 2013b. Rapid postseismic strength recovery of Pingxi fault gouge from the Longmenshan fault system: experiments and implications for the mechanisms of high-velocity weakening of faults. J. Geophys. Res. 118, 4547–4563. http://dx.doi.org/10.1002/jgrb.50308.

Yao, L., Ma, S., Platt, J.D., Neimeijer, A.R., Shimamoto, T., 2016. The crucial role of temperature in high-velocity weakening of faults: experiments on gouge using host blocks with different thermal conductivities. Geology 44 (1), 63–66.